NAM

Local and Moment Magnitudes in the Groningen Field

Bernard Dost, Ben Edwards and Julian J Bommer

Datum June 2016

Editors Jan van Elk & Dirk Doornhof

General Introduction

The magnitudes of the induced earthquakes in the Groningen field are assigned by the official seismological service of the Netherlands, which is part of the Royal Netherlands Meteorological Institute (KNMI).

These are local magnitudes, usually represented by the symbol M_L. Local magnitude was the first modern instrumental scale proposed and, after its author, it is sometimes referred to as Richter magnitude. Within the context of the Groningen seismic hazard and risk models, both the seismicity model (i.e. recurrence relationships) and the ground-motion prediction equations (GMPE) are being developed in terms of local magnitudes, which until now have been assumed equivalent to moment magnitude, M.

In this report the relationship between these two magnitude scales is derived. This is also important when comparing results from Groningen studies with experience and study results for earthquakes elsewhere.

NAM

Title	**Local and Moment Magnitudes in the Groningen Field.**		**Date**	June 2016
			Initiator	NAM
Author(s)	Bernard Dost, Ben Edwards and Julian J Bommer	**Editor**	Jan van Elk Dirk Doornhof	
Organisation	Academic Experts with KNMI	**Organisation**	NAM	
Place in the Study and Data Acquisition Plan	Study Theme: Seismological Model Comment: The magnitudes of the induced earthquakes in the Groningen field are assigned by the official seismological service of the Netherlands, which is part of the Royal Netherlands Meteorological Institute (KNMI). These are local magnitudes, usually represented by the symbol M_L. Local magnitude was the first modern instrumental scale proposed and, after its author, it is sometimes referred to as Richter magnitude. Within the context of the Groningen seismic hazard and risk models, both the seismicity model (i.e. recurrence relationships) and the ground-motion prediction equations (GMPE) are being developed in terms of local magnitudes, which until now have been assumed equivalent to moment magnitude, M. In this report the relationship between these two magnitude scales is derived. This is also important when comparing results from Groningen studies with experience and study results for earthquakes elsewhere.			
Directly linked research	1. Development of the Seismological Model 2. Ground Motion Prediction.			
Used data	Seismic Records from the Groningen field obtained by the KNMI Geophone and Accelerometer Network			
Associated organisation	KNMI			
Assurance	Internal and KNMI			

Local and Moment Magnitudes in the Groningen Field

Bernard Dost, Ben Edwards and Julian J Bommer

4th March 2016

TABLE of CONTENTS

1. Introduction

Gas production in the Groningen field in the northernmost part of the Netherlands is inducing earthquakes that potentially pose a threat to the built environment and to local inhabitants. As part of the response to the induced seismicity, a probabilistic seismic hazard and risk model is being developed for the Groningen field. An important element of this study is the quantification of earthquake size, which is generally expressed in terms of magnitude. There are several scales on which magnitude can be measured and these will often yield different values of the magnitude for a single earthquake.

1.1. Statement of the Problem

The magnitudes of the induced earthquakes in the Groningen field are assigned by the official seismological service of the Netherlands, which is part of the Royal Netherlands Meteorological Institute (KNMI). These are local magnitudes, which are usually represented by the symbol M_L. Local magnitude was the first modern instrumental scale proposed and, after its author, it is sometimes referred to as Richter magnitude (see Section 1.2.1). Within the context of the Groningen seismic hazard and risk models, both the seismicity model (*i.e*., recurrence relationships) and the ground-motion prediction equations (GMPE) are being developed in terms of local magnitudes, which until now have been assumed equivalent to moment magnitude, **M** (see Section 1.2.2). Although this assumption represents a reasonable starting point, for the final hazard and risk models it is considered imperative to explore and validate the assumed equivalence of the magnitude scales; if the assumption is found not be supported by the available data, then it may be that a transformation other than 1:1 will need to be applied to the KNMI magnitudes.

Although it is important, for completeness and for rigour, that the issue of the magnitude scales is addressed in detail, it is also worthwhile putting the issue into context. The GMPEs are being developed using a combination of stochastic simulations—using source, path and site parameter values estimated from inversions of the Fourier spectra of recordings obtained in the field—for the median predictions and local recordings to constrain the associated variability (expressed as the logarithmic standard deviation, generally referred to as sigma). No data are being used from other regions—with the possible exception of global models for the so-called single-station within-event variability and the models for the sigma correction due to the use of a point-source assumption (Bommer *et al*., 2015b; Bommer *et al*., 2016)—and there is also no intention to make the GMPEs transportable to any application other than the Groningen field. Additionally, comparisons may be made with data and models from other regions, and although these are not an essential element of the model-building process it is important that such exercises do not convey distorted views due to any systematic differences in the magnitude scales.

Moreover, stochastic simulations are at the core of the GMPE development and the scaling implicit in such approaches is scaling of ground-motion amplitudes with seismic moment (e.g. Boore, 2003). Should the relationship between M_L and **M** have a gradient other than unity, then this assumption in the stochastic simulations would be invalidated.

The Groningen GMPEs are therefore internally consistent in their use of magnitudes. Since the earthquake catalogue from which the recurrence relationships are derived is expressed in terms of the same magnitudes as those used to characterise the strong-motion recordings, there is also no issue of incompatibility in terms of the hazard calculations. The only issue that may be of significance would be if it were found that there were a non-linear relationship between M_L and **M** for the Groningen field, since this would have implications for the derivation of the Gutenberg-Richter (G-R) recurrence parameters: the G-R recurrence relationship is assumed linear and in the case of a non-linear relationship between the magnitude scales, this assumption would be invalid for one of the scales. Additionally, physically-based estimates of the maximum magnitude, M_{max}, defined in terms of moment magnitude would need to be adjusted to M_L if the assumed equivalence were found not to hold.

Notwithstanding that the issue of the magnitude scales is therefore not of overarching importance for the Groningen hazard and risk study (although 1:1 proportionality—rather than equivalence—is a key implicit assumption in the GMPE development), we consider it important nonetheless to investigate in detail the relationship between local and moment magnitudes in this region. The issue is addressed by first reviewing how the two magnitude scales (M_L and **M**) are defined, which is covered in Section 1.2. Section 2 then provides a comprehensive review of studies that have addressed the relationship between these two magnitude scales, including both empirical and theoretical publications as well as examples from other seismic hazard analysis projects. Section 3 then explores the specific case of Groningen, including an evaluation of local procedures at KNMI to determine magnitudes on both of the scales. Conclusions regarding the recommended procedures to be adopted for the Groningen hazard and risk assessments are summarised in Section 4.

1.2. Magnitude Definitions

Earthquake magnitudes provide a quantitative measure of size in terms of either a characteristic of the causative fault rupture itself or the energy radiated from this source. The two magnitudes that are the subject of this report, the local and moment magnitudes, are described in the following sections.

1.2.1. Local Magnitude

The local magnitude scale, also widely known as the Richter scale, is defined by the peak displacement on a specific type of seismometer, the Wood-Anderson seismometer, at a distance of 100 km from the earthquake. It is effectively a measure of the high-pass filtered displacement field resulting from the earthquake. The local magnitude scale was originally defined by Richter (1935) using recordings of earthquakes in California. He proposed that:

$$M_L = \log_{10} A - \log_{10} A_0 \quad (1)$$

with A the peak amplitude on a x2800 gain Wood-Anderson torsion seismometer in mm, and A_0 a correction for attenuation with distance [($\log_{10} A_0(100\ km) = -3$].

The attenuation correction was determined by Richter (1935) for California, using a small dataset of recorded events and was limited to an epicentral distance range of 30-600 km. Boore (1989), using a much larger dataset, showed that systematic differences of up to 0.4 magnitude units can be obtained at short distances (0-30 km) if no proper attenuation function for the region is derived. Other magnitude scales (M_S, surface wave, or m_b body wave) were developed to extend the magnitude scale to larger distances (> 600km) (Gutenberg and Richter, 1945a, 1945b).

The Wood-Anderson seismometer was commonly used at the time to record regional and local seismicity. However, it has a particular feature that has a direct influence on the local magnitude. That is the fact that the instrument is only sensitive to ground motion displacements above ~1 Hz. Below this frequency, the instrument's sensitivity rapidly diminishes; the seismometer itself therefore acts as a high-pass filter on the recorded displacement. The sensitivity of seismometers to ground motion can be quantified through the instrument response function, an example of which is given in Figure 1. The response of a Wood-Anderson seismometer means that the scale saturates for large earthquakes: for increasingly large events, the dominant frequencies of ground motion become increasingly small. Beyond magnitude 7 the dominant frequencies fall below the high-pass filter effect of the seismometer, meaning that the recorded motion does not increase at the same rate as for smaller events.

Despite the shortcoming of saturation at large magnitude, the local magnitude has been universally adopted as the magnitude of choice for regional earthquake observatories because it is easy and fast to calculate. Since the original scale was developed in California, where the geologic setting can be vastly different to other regions, most seismic observatories recalibrate the attenuation correction based on locally recorded seismicity. Whilst this should lead to a consistent magnitude scale, it typically does not, with regional differences becoming apparent where seismicity lies at the border regions of seismic networks (Fäh *et al.*, 2011). For instance, it is common for systematic differences between local magnitudes assigned by different

agencies: the French network LDG typically estimates French-Swiss border region events to be 0.4 units higher than the Swiss Seismological Service (SED). This is due to the simplistic nature of the attenuation correction, lack of consideration of site effects and different interpretations of 'peak Wood-Anderson displacement'.

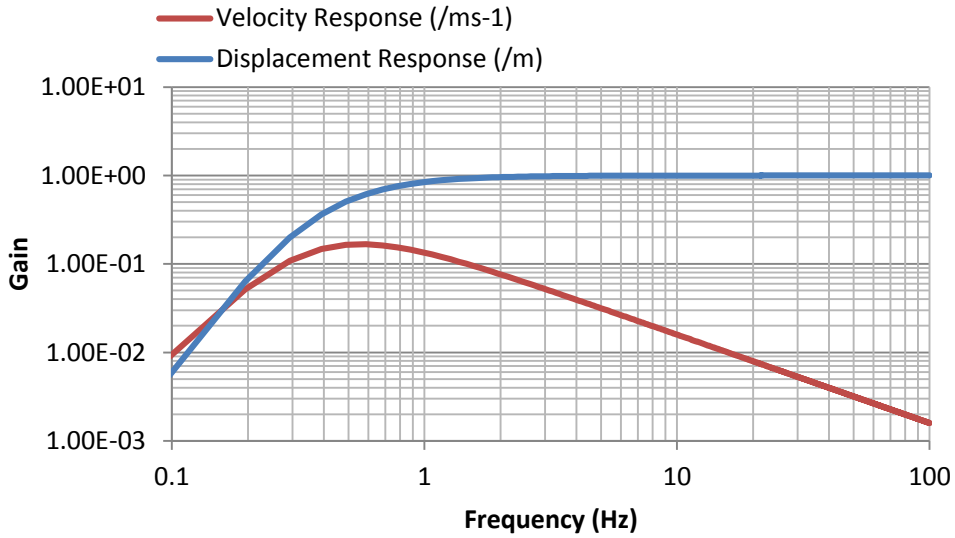

Figure 1: Example instrument response function of a Wood-Anderson seismometer.

1.2.2. Moment Magnitude

The moment magnitude is a measure of the size of the seismic moment (M_0) of an earthquake. The seismic moment has a physical definition that is based on the fault ruptre surface area (S) and displacement (d), and the shear-modulus of the material (μ):

$$M_0 = \mu S d \tag{2}$$

Using the Gutenberg and Richter (1956) magnitude-energy relation:

$$\log(\mathrm{E_s}) = 1.5\mathrm{M_s} + 11.8 \tag{3}$$

and noting that $\mathrm{E_s}$ (in Joules) could be replaced by a measure of the strain work done (W), Kanamori (1977) proposed an extension to the surface-wave magnitude that did not saturate due to band-limited recordings:

$$\log(\mathrm{W}) = 1.5\mathrm{M_w} + 11.8 \tag{4}$$

Kanamori (1977) showed that under certain assumptions $\mathrm{W} = M_0/2 \times 10^4$, such that the magnitude could be directly related to the seismic moment (in dyn.cm):

$$\mathrm{M}_w = \frac{2}{3}(\log_{10}(M_0) - 16.1) \tag{5}$$

In SI units, with dyn.cm = 10^{-7} Nm, the equation becomes:

$$\mathrm{M}_\mathrm{w} = \frac{2}{3}(\log_{10}(M_0) - 9.1) \tag{6}$$

Extending this concept by also noticing the concurrence of the equation for $\mathrm{M_L}$ in California (Thatcher and Hanks, 1973), Hanks and Kanamori (1979) defined the moment magnitude, uniformly valid from $3 \lesssim \mathrm{M} \lesssim 7,\ 5 \lesssim M_s \lesssim 7.5$ and M_w above as:

$$\mathbf{M} = \frac{2}{3}\log_{10}(M_0) - 6.07 \tag{7}$$

2. Overview of Literature

The following section provides an overview of existing literature on the topic of the relationship between local and moment magnitudes.

2.1. Studies Based on Empirical Data

Since both local and moment magnitudes are often directly determined for moderate sized earthquakes (4<**M**<6), there is the opportunity to observe, empirically, the relationship between the two. Unfortunately the magnitude range over which both magnitudes are available is often rather small due to the fact that moment tensor analyses (used to calculate **M**) require long-period waveforms (e.g., T > 10 s). For earthquakes below **M** = 4, these periods are typically dominated by noise. Some studies extend the lower limit of moment magnitude determination using spectral analysis techniques. A limitation in this case is that since short-period motions are analysed, there is a higher degree of uncertainty and the risk of biased estimates, for example due to local site amplification effects. Furthermore, methodological differences between approaches can lead to systematic bias in estimated magnitudes.

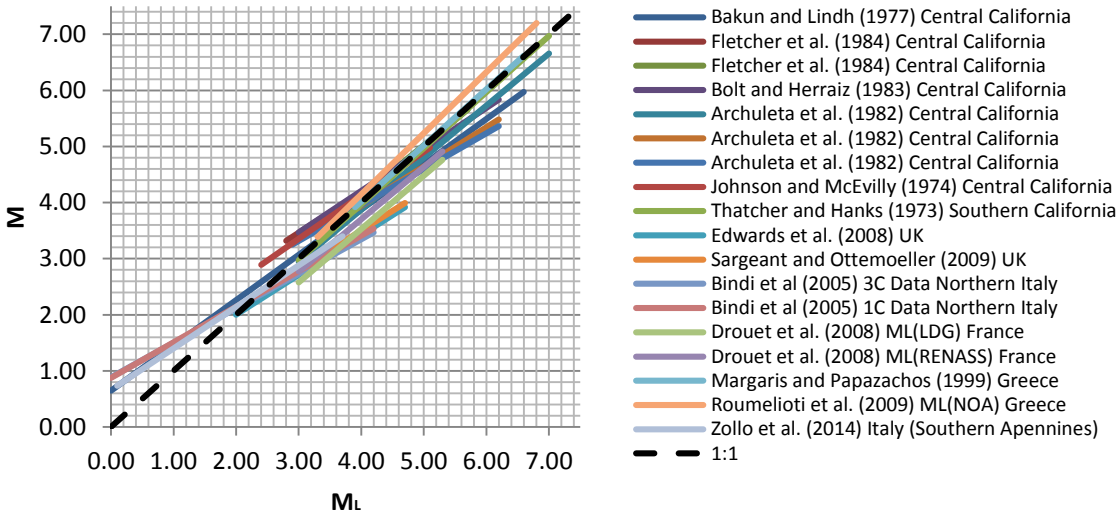

Figure 2: Comparison of several regional studies between M_L and **M** (;, Fletcher *et al.*, 1984; Bolt and Herraiz, 1983; Archuleta *et al.*, 1982; Johnson and Mcevilly, 1974; Thatcher and Hanks, 1973; Edwards *et al.*, 2008; Sargeant and Ottemoller, 2009; Bindi *et al.*, 2005; Drouet *et al.*, 2008; Margaris and Papazachos, 1999; Roumelioti *et al.*, 2009; Zollo *et al.*, 2014).

There are numerous studies comparing regional M_L and **M**. Often a shortcoming of such studies is the limited magnitude range available: regions of low seismicity, such as Northern Europe tend to focus on smaller magnitude data, using spectral analyses to obtain **M** from short-period data, while regions of higher seismicity tend

not to compute (or provide) moment magnitudes for smaller events. Authors therefore often use a simple linear regression (straight line fit) between the two magnitudes. Figure 2 shows a collection of such regressions

Authors have, in the past, assumed that **M** = M_L or that **M** = M_L + *a*. As seen in Figure 2, while this is a reasonable average assumption for M > 3: below this **M** tends to be systematically higher than M_L. In addition, individual regions show significant systematic differences, even for M > 3.

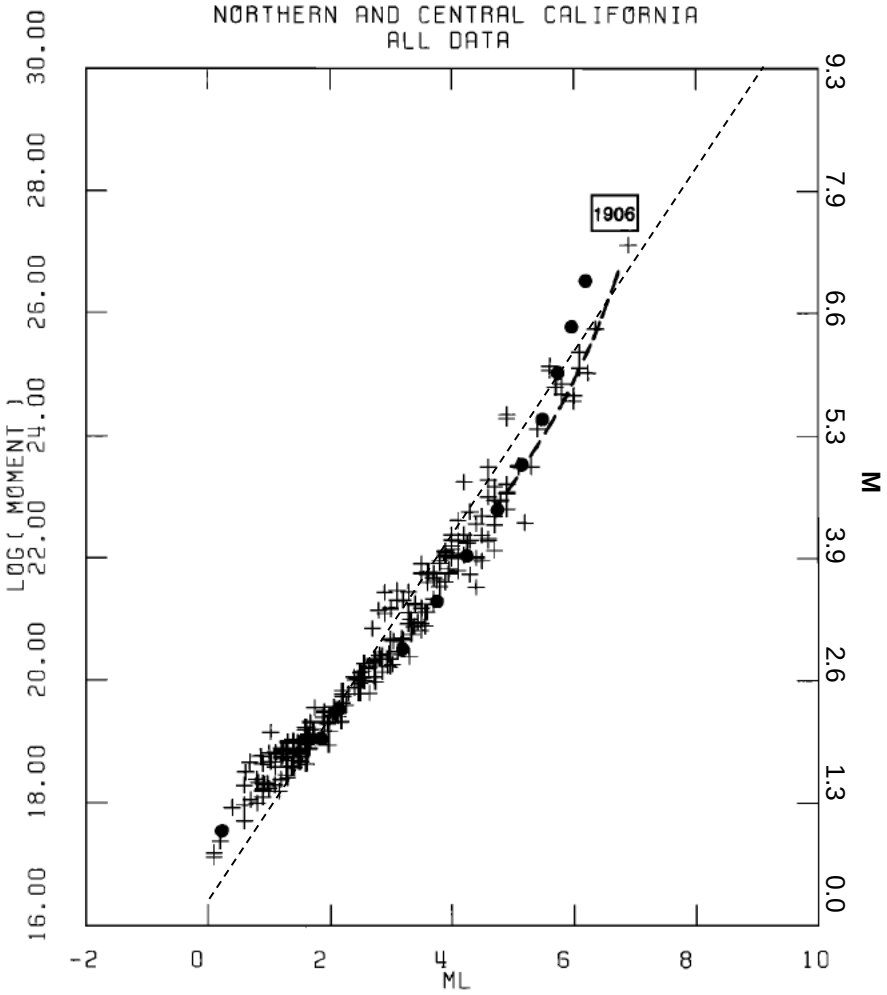

Figure 3: Moment magnitude data for central California earthquakes (crosses, box for the 1906 earthquake) and model calculations after Boore (1983) (solid circles, heavy dashed line for [the high magnitude] correction (Hanks and Boore (1984) Equation (4)). See Hanks and Boore (1984) for data sources. The lightweight dashed line indicates **M**=M_L. (Modified after Hanks and Boore (1984), Figure 2)

Due to the limits of computing **M** across a wide range of magnitudes, there are fewer studies that span the 'complete' range of magnitudes and investigate the magnitude dependence of the M_L:**M** scaling. An early example was that of Hanks and Boore (1984). They saw the variety of different scaling relations, even in the California

region (Figure 2), as evidence that the results depended on the chosen magnitude range. They analysed earthquakes between M_L = 0 and 7 from a number of sources. They observed a curvilinear relationship between M_0 (and consequently **M**) and M_L (Figure 3).

Grünthal et al. (2009) produced an earthquake catalogue for central, northern, and north-western Europe. Based on this they observed a quadratic trend between **M** and M_L (Figure 4). Similarly Edwards et al. (2010) used Swiss and border region (Italy, France, Austria, Germany) events to develop empirical relationships between M_L (assigned by SED) and **M** calculated based on spectral fitting (Figure 5).

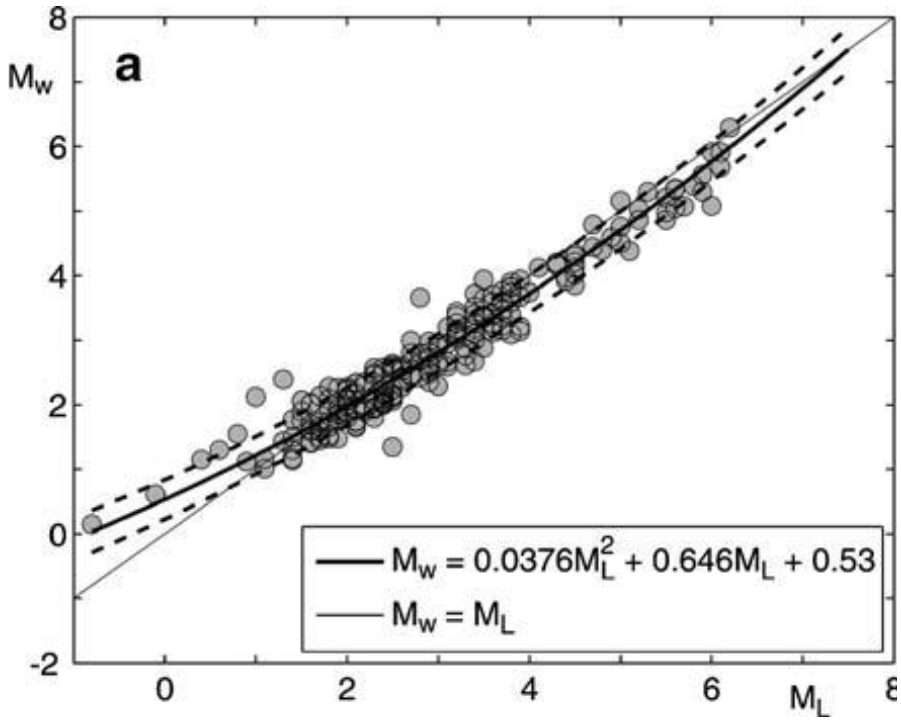

Figure 4: A) The updated **M**–M_L relations for central Europe based on data in (Grünthal and Wahlstrom, 2003) extended by new data (in total 221 data points; the dashed lines denote the 68% confidence bounds). (Figure 2 from Grünthal *et al*. (2009)).

Following Edwards et al. (2010), Goertz-Allmann et al. (2011) expanded the Swiss dataset to include events of smaller magnitude, and used moment tensor solutions for **M** where available (Figure 6). They defined a piecewise relationship (which is linear to M_L = 2, quadratic between M_L = 2 and 4, and then 1:1 scaling with **M** above M_L = 4) to avoid the problem of sparse data at low and high magnitudes.

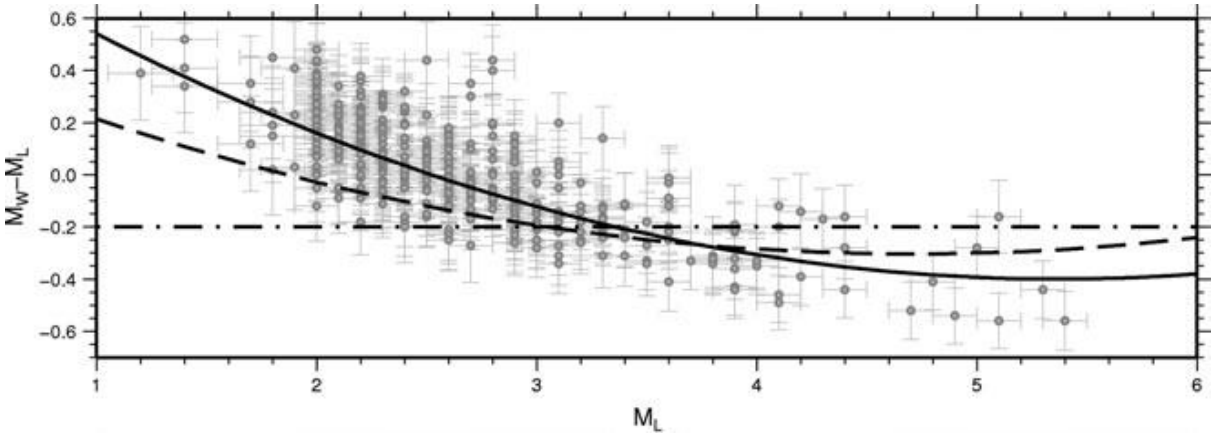

Figure 5: Plot of all events used to define the scaling relation. The M_L error bars indicate the standard deviation in M_L [$\sigma(M_L)$] as given by the earthquake catalogue of Switzerland (0.15 for $1 \leq M_L < 2$ and 0.1 for $M_L \geq 2$). The **M**–M_L error bars are given by ($\sigma^2 M_L + \sigma^2$**M**). The solid lines indicate the best model given by eq. (17 [in Edwards *et al.* 2010]), the dash-dot line indicates the old linear scaling relation (eq. 15 [in Edwards *et al*. 2010]) while the dashed lines indicate the scaling relation of Grünthal *et al*. (2009) [see Figure 4]. (Figure 6 from Edwards *et al*. (2010)).

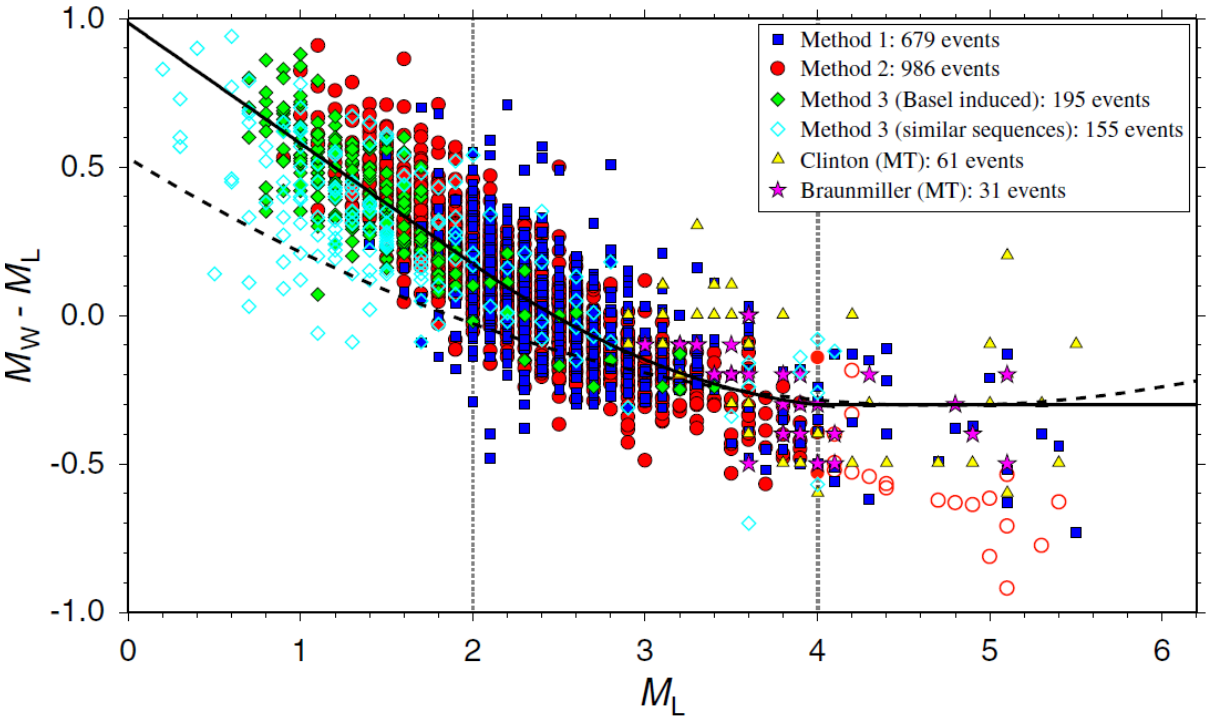

Figure 6: Difference between M_L and M_w versus M_L of three spectral methods and of MT inversions by the SED (Clinton *et al*., 2006) and Braunmiller et al. (2005). The combined scaling relation from three different segments is shown (solid line, see Table 1 of Goertz-Allmann *et al*., 2011). Open circles show data of method 2, which may be affected by saturation. The scaling relation obtained by Grünthal *et al*. (2009) is also included (dashed line). (Figure 4 in Goertz-Allmann *et al*. (2011)).

2.2. Simulation- and Theoretical-based Studies

Deichmann (2006) proved that **M** ∝ M_L in the absence of attenuation and neglecting the effect of the Wood-Anderson response. He did this by showing that as the seismic moment increases two things happen to the radiated displacement pulse: its duration increases, and its peak amplitude increases. The duration of the pulse is directly linked to the size of the fault, which can itself be related to the seismic moment and the static stress drop. After accounting for the increase in displacement pulse duration due to fault growth, it is shown that the peak amplitude must increase as 2/3(logM_0). Since **M** also increases with 2/3(logM_0), it can therefore be inferred that **M** = M_L + C. In practice therefore, assuming suitable calibrated scales, **M** = M_L.

Deichmann's initial analysis did not explain empirical observations (e.g., Figure 2). He argued that this could be to two issues: the effect of anelastic attenuation, or the instrument response, both of which were initially ignored. He then provided time-domain simulations showing the effect of Q and the Wood Anderson instrument (Figure 7). Figure 7 shows that for increasingly small **M**, the difference between M_L and **M** increases, just as in the empirical analyses. We further see that for larger events (**M** > 4), the effect of the Wood-Anderson instrument response also causes the **M** versus M_L plots to deviate from 1:1 (note the inverted axes compared to other plots in this report).

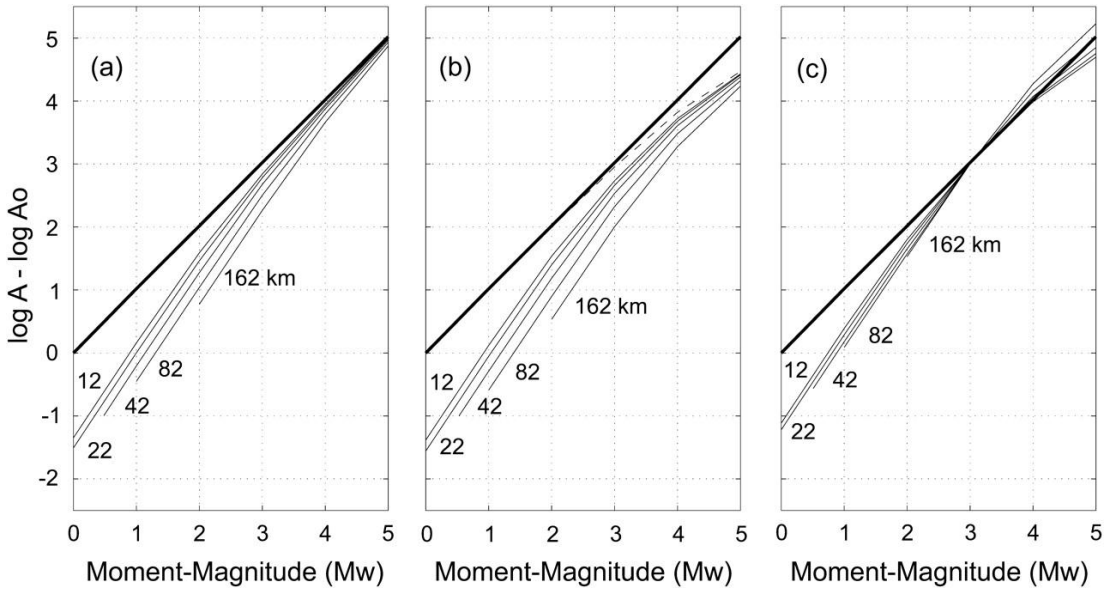

Figure 7: Normalized maximum displacement [log A – log A_0 ∝ M_L] versus moment magnitude. The heavy straight line corresponds to the unattenuated peak amplitude of the computed moment-rate functions. The light continuous curves give the expected relative amplitudes for the source and attenuation models discussed in the text of Deichmann (2006), at distances of 12, 22, 42, 82, and 162 km: (a) only the effect of *Q*, (b) *Q* and the influence of the Wood- Anderson seismograph, (c) like (b) but normalized to M_w 3. The dashed curve in (b) shows the effect of the Wood-Anderson seismograph alone. Figure 3 from Deichmann (2006).

In addition to time-domain simulations, random vibration theory (RVT) can be used to simulate the response of a Wood-Anderson seismometer to input ground motion. This was the method used by Hanks and Boore (1984, circles in Figure 3) to explain the curvature of the M_L:**M** data observed in their empirical analysis. Edwards et al. (2010) showed a number of examples (e.g., Figure 8) using this approach, with different input ground motion (defined by the **M**, stress-drop and Q). They showed that the form of the curvature was explained by different Q values (or equivalently site κ_0) at the low magnitude range, with the shape in the high-magnitude range (**M** > 5) defined by the stress-drop.

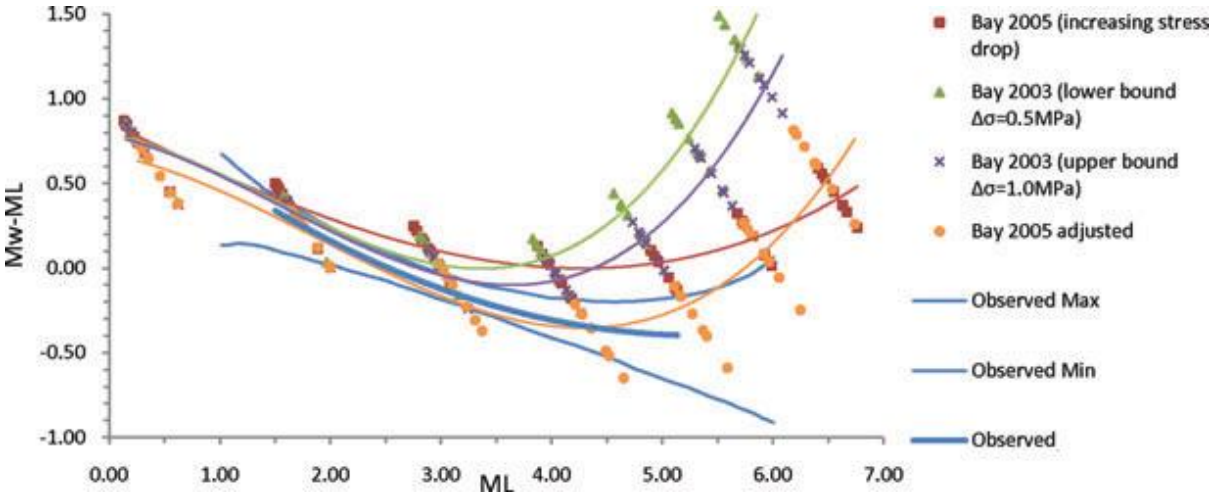

Figure 8: Synthetic M_L–**M** scaling relations based on the Bay *et al.* (2003, 2005) studies along with the adjusted Bay et al. (2005) gridsearch results. M_L values are computed for a range of distances, resulting in the observed scatter. Third degree polynomials are fit to the data to highlight the trend. The observed M_L–**M** scaling relation is included for comparison. Figure 8 of Edwards et al. (2010).

Both simulation analyses of Deichmann (2006) and Edwards et al. (2010) support the conclusion of Hanks and Boore (1984) that the scaling of M_L and **M** is due to a complex interaction of the earthquake source, wave-propagation and the response of the Wood-Anderson seismometer.

2.3. Approach in Previous Projects

Several hazard projects over the last decade have faced the issue of magnitude scaling. In the following sections the approach taken in these studies is briefly summarised.

2.3.1. PEGASOS/PRP

The PEGASOS Project (Probabilistic Seismic Hazard Analysis for Swiss Nuclear Power Plant Sites) was set up to assess the seismic hazard at nuclear power plant sites in Switzerland. As part of the project an update of the national earthquake catalogue was made (ECOS02: Earthquake catalogue of Switzerland, 2002), which in the case of no direct measure of **M** used a simple relation between M_L and **M**:

$$\mathbf{M} = \mathrm{M_L} - 0.2 \tag{8}$$

This was based on analysis of a catalogue of moment tensor based **M** and corresponding M_L in and around Switzerland (Braunmiller *et al.*, 2005).

A subsequent project, which aimed to refine the results of the PEGASOS Project (the PEGASOS Refinement Project, or PRP), was undertaken between 2007 and is currently under review by the regulator. As part of the project a revised earthquake catalogue was compiled (ECOS09). For this catalogue **M** was again assigned based on a scaling relation with M_L, but now using the curvilinear form of Goertz-Allmann et al. (2011):

$$\begin{aligned} \mathbf{M} &= 0.594\mathrm{M_L} + 0.985 && M_L < 2 \\ \mathbf{M} &= 1.327 + 0.253\mathrm{M_L} + 0.085M_L^2 && 2 \leq M_L \leq 4 \\ \mathbf{M} &= \mathrm{M_L} - 0.3 && M_L > 4 \end{aligned} \tag{9}$$

as discussed in Section 2.1. Whereas—based on the empirical analyses—the PEGASOS values would have systematically underestimated **M** for increasingly small values, using this curvilinear function in PRP/ECOS09 **M** estimates were considered valid to small magnitudes (**M** ~ 1.5). Unfortunately this brought to light a related issue: that if the Gutenberg-Richter (1944) (G-R) recurrence model (a linear fit to the logarithm of the cumulative number of events versus magnitude) is valid for M_L, then it is not (due to the curved scaling) valid on **M**, or vice-versa. Over regional scales, M_L does seem to follow (statistically) the G-R model over a wide range of magnitudes, which opens the question of its suitability for predicting **M**, and additionally its physical basis. In order to overcome this issue, the a- and b-values in PRP were again calculated using only **M** greater than a selected value (as chosen by individual evaluator experts); the aim being to avoid the curved-region of the magnitude scaling function.

2.3.2. CEUS-SSC

The Central Eastern United States Seismic Source Characterization for Nuclear Facilities (CEUS-SSC) project developed a homogenised earthquake catalogue for the central and eastern US region (USNRC, 2012). The catalogue contained relatively few M_L and **M** pairs (Figure 9) but they did observe that "*the trend of the data on* [Figure 9, this report] *displays the typical flattening of slope at the lower magnitudes*." In order to avoid this issue, to "*minimize the influence of this flattening*

*on the estimation of **M** in the range of interest, the data below M_L 3.5 were not used in fitting the* [M_L versus **M**] *model*."

Additionally, in order to convert M_L to **M** the authors propose a number of different approaches depending on the data source and depending on the availability of data, for example:

- For events in the north-east region, it was assumed that $M_L = M_c$, where M_c is the coda magnitude.
- M_L magnitudes reported by the Southern California Seismic Network (SCSN) are equivalent to the M_c magnitudes reported by SCSN.
- M_L magnitudes reported by the Advanced National Seismic System (ANSS) in the vicinity of New Madrid are equivalent (with minor exception) to M_D (duration magnitude) reported by the Center for Earthquake Research and Information (CERI) for $M_D > 3$.

These converted magnitudes were then in turn converted to **M** through more robustly determined conversion equations. This procedure, nevertheless added significant uncertainty, with standard errors of 0.3 to 0.4 magnitude units.

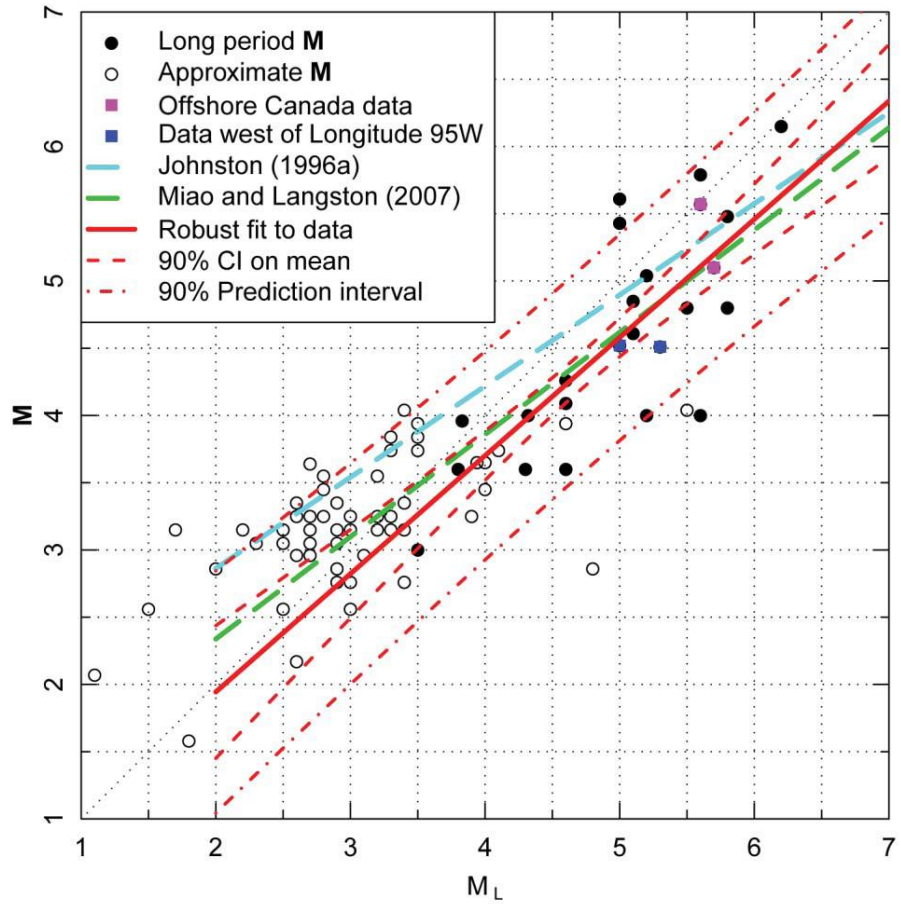

Figure 9: M_L:**M** data from the CEUS SSC Project catalog and robust regression fit to the data. (Figure 3.3.22 from the CEUS SSC Final Report (USNRC, 2012))

2.3.3. *Thyspunt PSHA*

The Thyspunt PSHA Project was a site-specific hazard analysis for a South African nuclear power plant site. As part of the project a homogeneous earthquake catalogue was compiled, with magnitude in **M**. In order to provide estimates of **M** where direct measures were unavailable, conversion equations were developed (Strasser, 2013). Since a wide range of magnitudes were available with both **M** and M_L, she developed a South Africa specific equation. The equation was developed giving strong preference to fitting the larger events with available moment tensors, whilst avoiding sharp jumps. This led to a correction that tends to systematically overestimate **M** for a range of magnitudes (3 to 4). However, the PSHA was only carried out for M_{min} = 5 (Bommer *et al.*, 2015a) so this was not considered relevant.

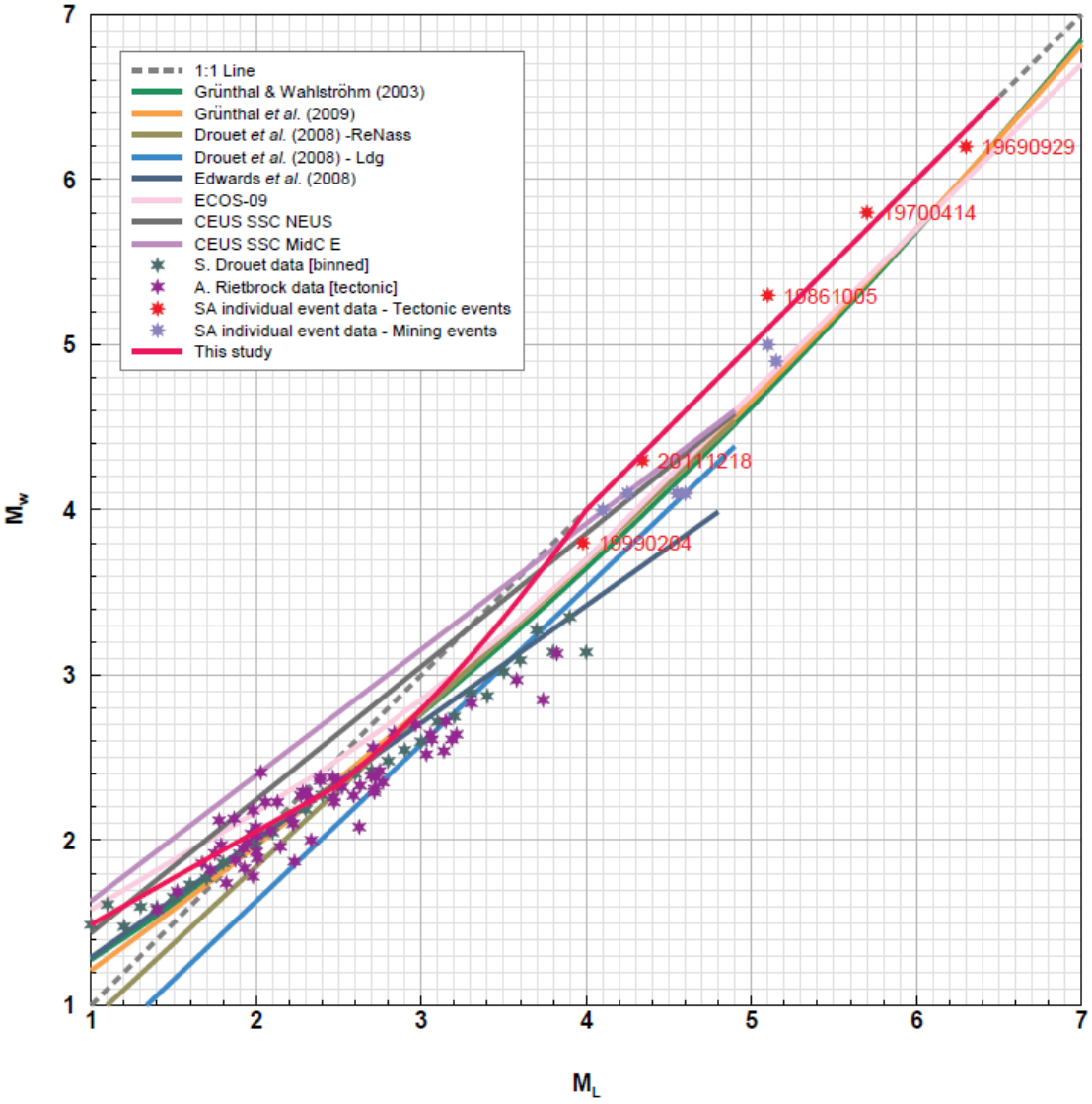

Figure 10: **M** versus M_L for South African earthquakes using a number of approaches along with the M_L:**M** conversion equations of other authors and the model used for South Africa (red line). (Figure 4 of Strasser (2013))

2.3.4. SHARE

The Seismic Hazard Harmonization in Europe (SHARE) Project developed an earthquake catalogue for the European region. Due to the diversity of data sources (individual country seismic networks and observatories) different conversions were applied to M_L to obtain **M**. The conversions are too numerous to describe in detail in this context, but can be found in Grunthal and Wahlstrom (2012) and Grunthal *et al.* (2013). The majority of conversions from M_L relied on a linear scaling of the general form $\mathbf{M} = aM_L + b$, for example:

$\mathbf{M} = 0.65M_L + 1.90$	Caucasus/Eastern Turkey $4 \leq M_L \leq 7$	(10)
$\mathbf{M} = 1.31M_L - 1.44$	France (LDG) $M_L < 4.65$	
$\mathbf{M} = M_L$	France (LDG) $M_L \geq 4.65$	
$\mathbf{M} = 0.906M_L + 0.65$	Italy (INGV)	
$\mathbf{M} = 0.0376\mathrm{M}_\mathrm{L}^2 + 0.646M_L + 0.53$	Bulgaria	

3. The Groningen Case

Since the north of the Netherlands was apparently aseismic before the first induced event was recorded in the region, no local magnitude calibration was carried out. Only one short-period station (WIT) was in operation in the region since 1972 as part of the KNMI network. Since 1988 a monitoring network was built-up in two stages: the first one as a small aperture array around the city of Assen consisting of short-period vertical sensors located at the surface. Its purpose was to monitor only one small gas field. In a second stage a network of 3-component sensors located in boreholes was installed in 1995, replacing and extending the first array (Dost and Haak, 2007). In addition to the borehole monitoring network, a surface network was added consisting of accelerometers. Data from this network was used to calculate moment magnitudes.

3.1. Local Magnitude

The Assen network enabled a first determination of an attenuation curve for the region. Haak *et al*. (1992) measured the peak amplitude of the P-onset. Peak amplitudes were measured in counts and no instrument correction or simulation of a Wood-Anderson seismograph was applied. An attenuation curve was constructed of the form:

$$A_0(r) = c\, R^{-1}\, e^{-\alpha R} \qquad (11)$$

with c= 5500 counts, α= 0,005 km^{-1} , assuming that geometrical spreading behaves as R^{-1}, with R the hypocentral distance; this is assumed to be only valid for the instrumentation around Assen. This curve was constructed on the basis of an analysis of four events of magnitude 2.2 to 2.7 at epicentral distances between 5 and 50 km. The magnitude of the largest events was determined by stations in the southern part of the Netherlands.

In 1991 an experimental borehole station FSW was installed with four levels of 3-component geophones at 75m vertical spacing and data from a level at 225 m depth were used to determine magnitudes. The previous attenuation curves were extrapolated and used in interpretation of the borehole data, without further calibration since the dataset at that time was too small. Since 1995, eight borehole stations have been in operation in the region and the dataset has rapidly expanded, so a real calibration became possible.

Following Kanamori et al. (1993) the attenuation function was modelled using the function *q*(*R*):

$$q(R) = c\, R^{-n} e^{-\alpha R} \tag{12}$$

which includes effects of geometrical spreading, attenuation, reflection and refraction and scattering and is regarded as a reasonable description for short distances. Since there are existing estimates of M_L, based on the attenuation curve of Haak *et al*. (1992), a search was conducted for values of parameters *c*, *n* and α by minimizing the function

$$\phi = \sum_{j=1}^{N} \sum_{i=1}^{M} |\log A_{i,j} - M_{L_i} - \log q(R_j)|^2 \tag{13}$$

$$M_{L_i} = \frac{1}{N} \sum_{j=1}^{N} M_{L_{i,j}}$$

where index *i* refers to the event and *j* to the recording station and *A* is the Wood-Anderson simulated amplitude (half peak-to-peak).

There is a trade-off between *n* and α, which was noted by several authors (e.g. Bakun *et al.*, 1984; Savage *et al*., 1995). A grid search was carried out. After an initial estimate of the attenuation function, new values for M_L are calculated and a new minimization is performed to refine the estimate of the attenuation function. It is important to realize that amplitudes are measured at the deepest level in the boreholes at 200 m depth, with the exception of FSW (225 m depth). Based on a dataset of 157 records, recorded in 1995 and the first half of 1996, minimization of Equation (13) led to:

$$\log_{10} A_0 = -1.33 \log(R) - 0.00139\, R - 0.424 \tag{14}$$

The first term implies that geometrical spreading is more significant than the usual assumed $1/R$ and from the second term an average Q = 280*f (for β=3.5 km/s) can be derived (Bakun et al., 1984). The attenuation function applies to a larger region than only the Groningen area, since the network covers also many small gas-fields.

Equation (14) was used in determination of the local magnitudes. It was not updated after more records became available. Figure 11 shows the variation with respect to the average magnitude. For distances less than 10-15 km a distance dependence is observed and a correction of the attenuation relation may be considered as also found in other regions (e.g., Edwards *et al.*, 2015).

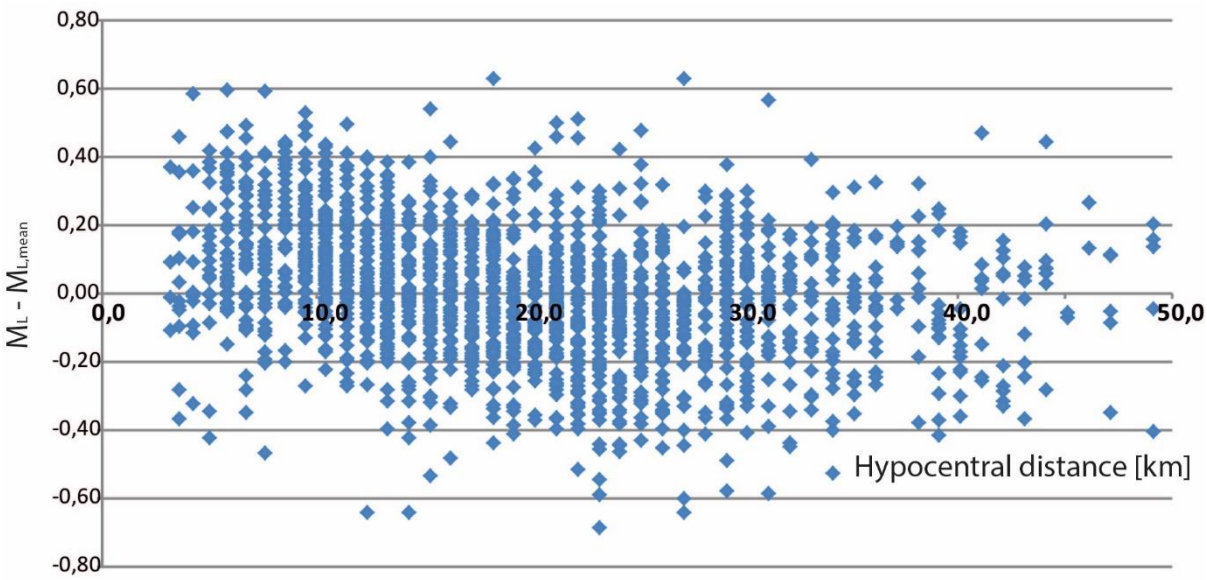

Figure 11. M_{Lj} - M_L for events recorded in the period 2010-2015 as a function of distance.

3.2. Moment magnitude

Seismic moment, M_o, can be derived from the spectra of P and S waves. In this report the focus is on S waves. The S-wave displacement spectrum A(f) recorded in one station can be written as the product of a source term, $\Omega(f)$, an attenuation term, $D(R,f)$ and a site effect term, $S(f)$:

$$A(f) = \Omega(f)D(R,f)S(f) \tag{15}$$

Where R is the hypocentral distance, f is frequency. As a source model the Brune, (1970, 1971) model is chosen, modified by Boatwright (1978):

$$\Omega(f) = \frac{\Omega_0}{\left(1+\left(\frac{f}{fc}\right)^{\gamma n}\right)^{1/\gamma}} \tag{16}$$

Abercrombie (1995), de Lorenzo *et al.* (2010) and others found that γ=2 and n=2 produces a better model for spectra of nearby earthquakes compared to the standard Brune model with γ=1 and n=2. One test of model fit to the Groningen data showed that this also applies to the current dataset. It is important to note, however, that overall the performance of the two source spectrum models are comparable and there is not a compelling reason to select one over the other, as discussed in the Appendix. The low-frequency spectral level Ω_0 can be expressed in terms of seismic moment M_0:

$$\Omega_0 = \frac{2\Phi}{4\pi\rho_0^{\frac{1}{2}}\rho_s^{\frac{1}{2}}v_0^{\frac{1}{2}}v_s^{\frac{5}{2}}} g(R)M_0 \tag{17}$$

where Φ denotes the average radiation, which is taken as 0.55 for shear waves (Boore and Boatwright, 1984), ρ_s the density at the source (2600 g/cm^3) and ρ_0 density at the surface (2100 g/cm^3), v_s the shear velocity at the source (2009 m/s, pers. comm. Remco Romijn) and v_0 shear velocity at the surface (200 m/s). The free-surface effect is introduced as a factor of 2, which is exact for near vertical incoming SH waves and in general a reasonable estimate for vertical incoming SV waves. The function $g(R)$ describes the geometrical spreading and will be discussed later. Attenuation along the path from source to receiver involves anelastic decay (e.g., Drouet *et al.*, 2010) and high-frequency damping:

$$D(r,f) = e^{-\frac{\pi R f}{Q v_{sa}}} e^{-\pi \kappa f} = e^{-\pi f t^*} \quad (18)$$

with $t^* = \frac{R}{Q v_{sa}} + \kappa_0$

where v_{sa} is the average shear velocity between source and receiver. Q is the damping parameter and in these calculations assumed to be frequency independent. S(f) is the site effect. Combining Equations (15) to (18), the S-wave spectral displacement can be written as:

$$A(f) = \Omega_0 \frac{S(f)}{\left(1+\left(\frac{f}{f_c}\right)^4\right)^{1/2}} e^{-\pi f t^*} \quad (19)$$

A grid search was carried out to determine the best fitting parameters for f_c, t^* and Ω_0 and calculate M_0. This grid search was carried out using a minimization function:

$$\sigma^2 = \frac{1}{N}\sum_{j=1}^{N}\left|\log(A^{obs}(f_j)) - \log(A^{calc}(f_j))\right|^2 \quad (20)$$

For each event, the spectrum of each station is processed separately, since this will give insight in the variability of the estimated parameters. Moment magnitude is calculated using Equation (6) where:

$$M_0 = \frac{4\pi\rho_0^{1/2}\rho_s^{1/2}v_s^{5/2}v_0^{1/2}}{2\Phi g(R)}\Omega_0 \quad (21)$$

This formulation assumes that *S*(*f*)=1, with frequency-independent amplification included in Equation (21) by accounting for the impedance contrast between the source and site.

3.3. Data and processing

The Groningen accelerometer network has developed over the years from a sparse stand-alone triggered system to a dense continuous recording system. The former consisted of SIG SMACH instrumentation (Dost and Haak, 2002), while the latter is equipped with Kinemetrics Episensor accelerometers and Basalt dataloggers. The triggered systems provide output in cm/s^2, while the Episensor data needs a conversion from digital counts. This conversion factor is 4.7684e-7 g/C and the response is flat for acceleration within the frequency range of interest (about 0.2 to 10 Hz although for risk analyses the dominant range is more like 2-10 Hz).

The data processed in this report have been recorded in accelerometer stations of the Groningen network. Data are sampled at 5 ms time intervals and recorded in real time as continuous mini-seed volumes and transferred over the Internet using the seedlink protocol. A time window of 512 samples (2.56s) around the S-onset was selected for processing. A Hanning window was applied prior to the Fourier transformation. Based on the signal-to-noise ratio of most records, the frequency range used to fit the measured spectra to the model is limited to 1-30 Hz (e.g., Figure 12).

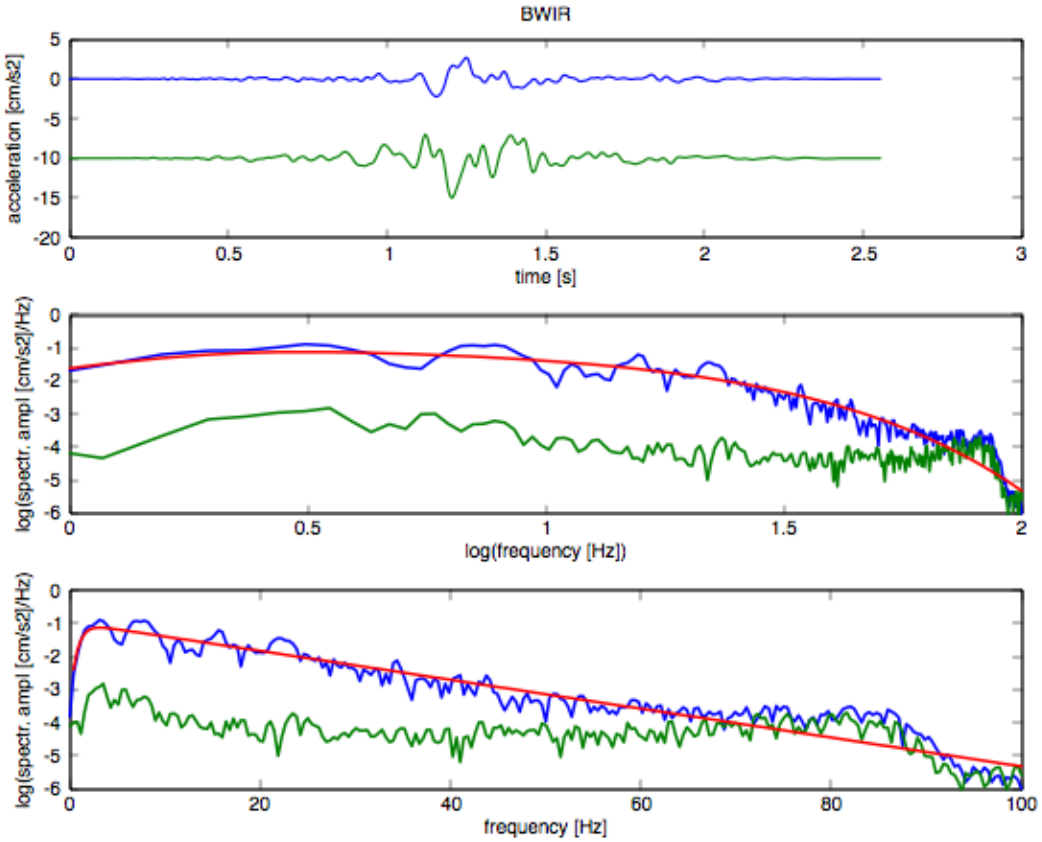

Figure 12: Example of processing. Top: acceleration data (east-west and north-south); Middle: Fourier spectrum (blue), model fit (red) and noise (green), logarithmic frequency axis. Bottom: same as middle, now showing a linear frequency-axis.

The geometric mean of the spectra of the horizontal components is used in this analysis, compatible with the development of the ground motion prediction equation (GMPE) for Groningen (Bommer *et al.*, 2016). In the process of spectral fitting a strong correlation between corner frequency, f_c, and attenuation, t^*, is observed. The estimate of the low-frequency part of the spectrum, Ω_0, is much more stable and is the only parameter required for calculation of **M**.

3.4. Geometrical spreading

In Equation (17) the geometrical spreading is usually assumed to be well described by a simple g=1/R relation. However, in the attenuation relation derived for the M_L calculation, a higher attenuation was found g= $R^{-1.33}$. For magnitude calculations this parameter is of crucial importance. Drouet *et al*. (2005) modeled geometrical spreading by:

$$g(R) = \frac{1}{R_0}\left(\frac{R_0}{R}\right)^{\gamma} \tag{22}$$

Where R_0 is equal to a reference distance. Since for the low-frequency part of the spectrum:

$$\log(A(r, f \to 0)) = \log\left(\frac{2\Phi M_0}{4\pi\rho_0^{1/2}\rho_s^{1/2}v_s^{5/2}v_0^{1/2}}\right) + \log\big(S(f \to 0)\big) - \gamma\log\left(\frac{R}{R_0}\right) \tag{23}$$

The parameter ɣ can be estimated from the distance dependence of measured Ω_o values. In this procedure R_0 = 1000 m. For the determination of an average geometrical spreading factor for Groningen, events of different magnitudes are compared by normalizing the logarithm of the low-frequency part of the spectrum with the logarithm of the averaged seismic moment for each event. Results are shown in figure 13. Linear regression gives an average geometrical spreading factor ɣ= 1.9.

A major source of error in these measurements is the effect of the radiation pattern and a possible site effect. Therefore, comparison with model calculations is important.

Results from finite difference, isotropic wave equation modelling (Bommer *et al.*, 2015b) are shown in Figure 14. A clear difference in geometrical spreading is observed for the hypocentral distance range 3-7 km and 10-14 km. It should be noted that this modelling is performed for elastic media. The average geometrical spreading derived from the normalized low-frequency spectra is in line with the modelling results.

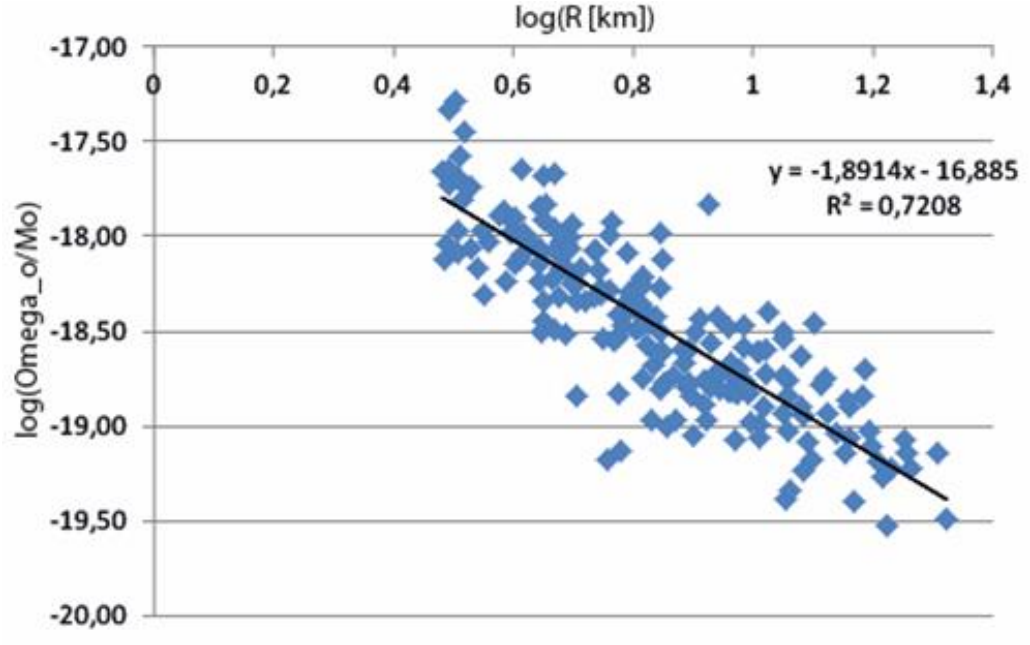

Figure 13. Distance dependence of the normalized low frequency spectral level for Groningen events listed in Table 1

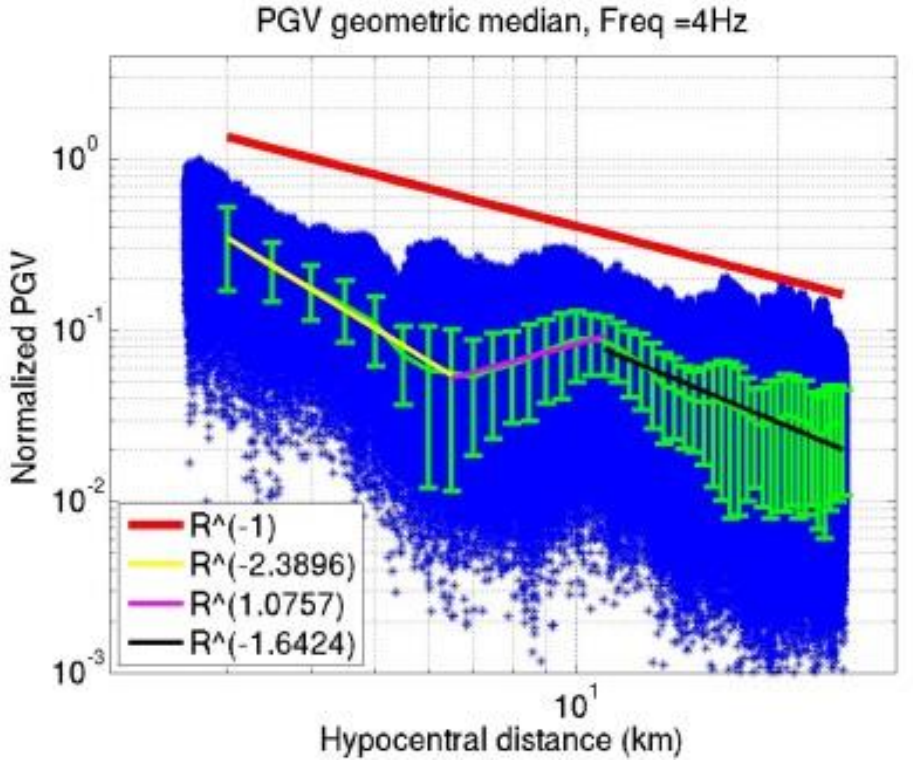

Figure 14. PGV as a function of distance for the Groningen area near Zeerijp (Bommer *et al.*, 2015b). Binned data is shown in blue, average values in green. Fits to particular distance ranges are shown along with the 1/R line for reference. Figure courtesy of Ewoud van Dedem.

For all events a general ɣ= 1.9 is used for each station in the calculation of **M**. However, for the Garmerwolde event (2014-09-30), with location in the south-west part of the field, this choice for geometrical spreading results in a clear increase of magnitude with distance. For this event, only recordings obtained at epicentral distances < 10 km have been used in the analysis.

3.5. Stress-drop

Since the stress-drop may be of influence on the magnitude relation, Brune's stress-drops are calculated using the relation:

$$\Delta\sigma = \frac{7}{16} M_0 \left(\frac{f_c}{0{,}37 v_s}\right)^3 \quad (24)$$

A stable estimate of the corner frequency for each event is essential in the calculation of the stress-drop. Since there are not many collocated events, the use of a method based on Empirical Green's functions (Viegas *et al*., 2010) could not be applied. We followed the authors in their approach to perform an individual spectral analysis determining the uncertainty range in f_c by a variance increase of 5%, keeping Ω_o and t^* as free parameters in the fit. For each event, data were selected from one station which showed the least complicated waveform and did have a corner frequency around the average observed.

3.6. Results

3.6.1 *Relation M_L-**M***

A total of 34 events, listed in Table 1, have been processed to calculate **M** and compare these values to measured M_L. In general the uncertainties in M_L are larger than uncertainties in **M.** This may be caused by the fact that the original borehole network has a large inter-station distance (on average 20 km), while covering a heterogeneous upper crustal structure. The distance between the accelerometer stations is less and, being located at the surface, include the influence of the heterogeneous upper 200m.

Results from this limited dataset show for $M_L > 2.5$ a trend parallel to the line **M**=M_L, at an offset around 0.2 magnitude units (Figure 15). For $M_L<2.5$ this trend seems to vanish, although the dataset is still small.

Figure shows the results for Groningen in a plot similar to Figure 5 and Figure 6 to facilitate comparison. The uncertainties on both **M**-M_L and M_L are shown as error ellipses. Assuming a linear relation between the two parameters, the best fitting curve has been calculated, based on the method developed by York *et al.* (2004):

$$\boldsymbol{M} - M_L = bM_L + a \qquad (25)$$

with a= 0.327 ± 0.186 and b= -0.169 ± 0.071.

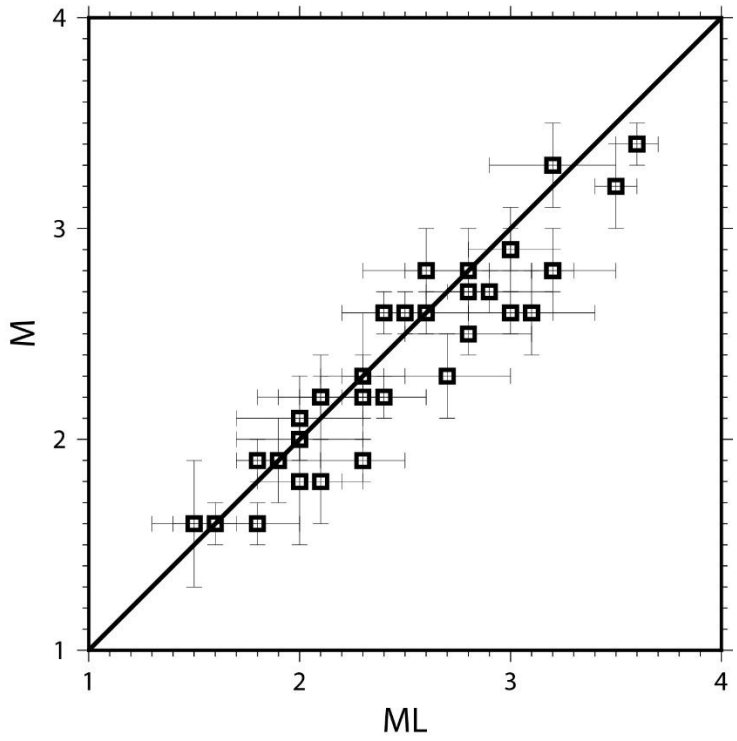

Figure 15. Moment magnitude **M** as a function of local magnitude M_L

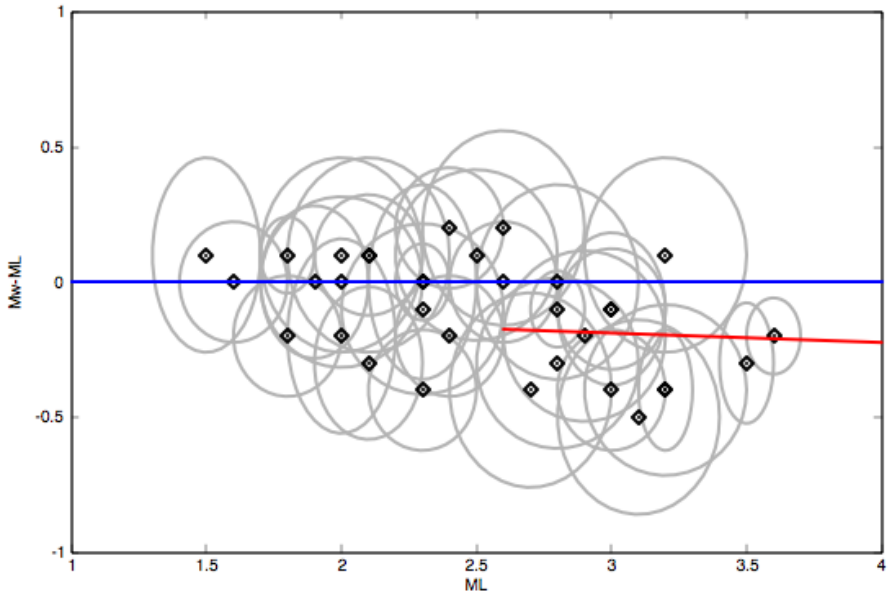

Figure 16. **M**-M_L as a function of M_L for the events listed in table1. Uncertainties are shown as ellipses. A linear regression for M_L > 2.5, taking into account uncertainties in both parameters, is shown in red.

Limiting the dataset to M_L>2.5, which is the lowest magnitude considered in probabilistic seismic hazard analysis for Groningen, the regression parameters become a = -0.084 ± 0.560 and b= -0.035 ± 0.181, which can be approximated for magnitudes 2.5<M_L<4 by:

$$\mathbf{M} = M_L - 0.2 \quad (26)$$

Table 1. Events used in the **M**-M_L calculations with their corresponding magnitudes

yymmdd	time	lat	lon	M_L	**M**	Name	# rec
060808	05:04:00.1	53.350	6.697	3.5 ± 0.1	3.2 ± 0.2	Westeremden	4
081030	05:54:29.1	53.337	6.720	3.2 ± 0.1	2.8 ± 0.2	Westeremden	6
090414	21:05:25.9	53.345	6.680	2.6 ± 0.2	2.6 ± 0.1	Huizinge	3
090508	05:23:12.0	53.354	6.762	3.0 ± 0.2	2.6 ± 0.1	Zeerijp	5
110119	19:39:31.7	53.319	6.645	2.4 ± 0.2	2.2 ± 0.1	Westerwijtw.	4
110627	15:48:09.6	53.303	6.787	3.2 ± 0.3	3.3 ± 0.2	Garrelsweer	8
110831	06:23:57.2	53.444	6.687	2.5 ± 0.3	2.6 ± 0.1	Uithuizen	3
120816	20:30:33.3	53.345	6.672	3.6 ± 0.1	3.4 ± 0.1	Huizinge	7
130119	20:10:06.5	53.285	6.790	2.4 ± 0.2	2.6 ± 0.1	Overschild	3
130207	23:19:09.0	53.389	6.667	3.2 ± 0.3	2.8 ± 0.1	Zandeweer	3
130702	23:03:55.5	53.294	6.785	3.0 ± 0.2	2.9 ± 0.1	Garrelsweer	2
130904	01:33:32.1	53.344	6.772	2.8 ± 0.1	2.7 ± 0.1	Zeerijp	5
140213	02:13:14.3	53.357	6.782	3.0 ± 0.2	2.9 ± 0.2	Leermens	14
140311	09:08:23.4	53.228	6.822	2.3 ± 0.2	2.3 ± 0.3	Schildwolde	5
140318	21:15:18.3	53.390	6.618	2.1 ± 0.3	2.2 ± 0.2	Rottum	6
140702	17:34:16.7	53.214	6.790	2.1 ± 0.2	2.2 ± 0.1	Slochteren	5
140809	15:55:32.9	53.325	6.835	2.0 ± 0.3	2.1 ± 0.2	Oosterwijtwerd	6
140901	07:17:42.9	53.194	6.787	2.6 ± 0.3	2.9 ± 0.2	Froombosch	6
140930	11:42:03.4	53.258	6.655	2.8 ± 0.3	2.8 ± 0.2	Garmerwolde	12
141105	01:12:34.5	53.374	6.678	2.9 ± 0.3	2.7 ± 0.1	Zandeweer	14
141230	02:37:36.7	53.208	6.728	2.8 ± 0.3	2.5 ± 0.1	Woudbloem	11
150106	06:55:28.2	53.324	6.768	2.7 ± 0.3	2.3 ± 0.1	Wirdum	12
150118	10:54:10.3	53.233	6.720	1.5 ± 0.2	1.6 ± 0.3	Lageland	6
150225	10:02:56.9	53.323	6.857	2.3 ± 0.1	2.3 ± 0.1	Appingedam	10
150324	13:27:56.8	53.322	6.855	2.3 ± 0.3	2.2 ± 0.1	Appingedam	10
150516	14:14:49.1	53.306	6.847	1.6 ± 0.2	1.6 ± 0.1	Appingedam	7
150521	21:08:47.7	53.244	6.810	1.8 ± 0.1	1.9 ± 0.1	Schildwolde	5
150527	10:52:10.0	53.404	6.668	2.0 ± 0.3	2.0 ± 0.1	Uithuizen	6
150606	23:39:15.x	53.340	6.750	1.9 ± 0.2	1.9 ± 0.2	Loppersum	9
150610	02:26:07.x	53.344	6.753	1.8 ± 0.2	1.6 ± 0.1	Zeerijp	9
150707	03:09:00.9	53.262	6.631	2.1 ± 0.2	1.8 ± 0.2	Thesinge	10
150818	07:06:12.6	53.185	6.754	2.0 ± 0.2	1.8 ± 0.3	Kolham	8
150930	18:05:37.2	53.234	6.834	3.1 ± 0.3	2.6 ± 0.1	Hellum	12
151030	18:49:01.1	53.285	6.920	2.3	1.9 ± 0.1	Meedhuizen	5

Regarding the data in Table 1, from 01-01-2014 onward, all events of $M_L \geq 2.0$ are selected, before that time only events of $M_L > 3.0$ and some additional smaller events have been selected. Starting in 2015 some events could be added with $M_L < 2.0$. The last column shows the number of records available for analysis.

3.6.2 Stress-drop

Figure 17 shows the results for the calculation of the stress-drop, listed in Table 2.

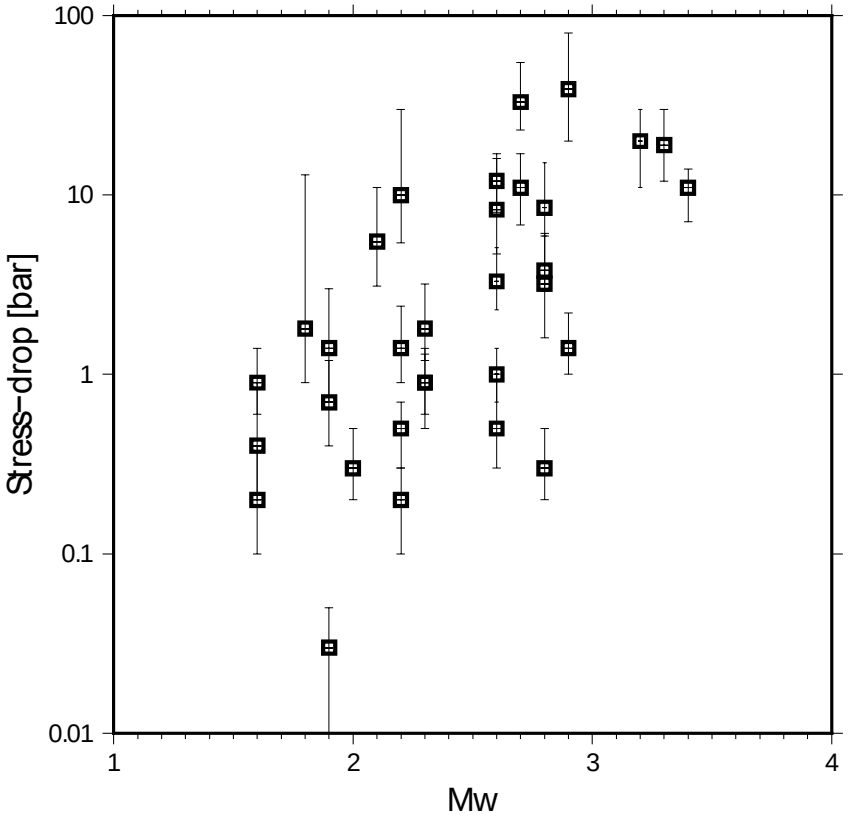

Figure 13. Overview of stress-drop measurements for Groningen events.

The majority of the Groningen events do show a low stress-drop ($\Delta\sigma$ < 20 bar). There is some indication for an increase in stress-drop with magnitude (**M**, see Figure 13) for **M**<3, although the dataset is small and the variation in stress drop large. The stress-drops presented are best estimates for each event evaluated in the reference station mentioned in table 2 (under the heading **stat**). Uncertainties are also listed in the table as minimum and maximum values of both stress-drops and corner frequency.

The largest stress-drop value (event 2014-02-13: $\Delta\sigma$ = 39 bars) has an uncertainty range of 20-80 bar. The current version of the GMPE (Bommer *et al.*, 2016) takes into account stress-drops up to 100 bar.

Table 2. Corner frequencies and stress-drops for events analysed. Parameter uncertainties are listed (min, max values) and the reference station used.

yymmdd	f_c-min	f_c	f_c-max	Δσ-min	Δσ	Δσ -max	stat	ML	**M**
060808	2.8	3.8	4.9	11.1	19.7	30.1	mid3	3.5	3.2
081030	3.2	3.9	5.1	5.9	8.5	15.1	wse	3.2	2.8
090414	1.6	2.0	2.4	0.7	1.0	1.4	mid3	2.6	2.6
090508	2.2	2.9	3.8	2.3	3.3	5.1	zan1	3.0	2.6
110119	5.4	7.4	11.2	5.4	10	30	mid1	2.4	2.2
110627	2.1	2.8	3.7	12	19	30	garst	3.2	3.3
110831	3.6	4.4	5.2	8	12	17	wse	2.5	2.6
120816	1.3	1.7	2.1	7.1	11	14	mid1	3.6	3.4
130119	1.0	1.7	2.6	0.3	0.5	1	hks	2.4	2.6
130207	1.8	2.2	2.6	2.9	3.8	5.9	kant	3.2	2.8
130702	1.3	1.7	2.3	1.0	1.4	2.2	win	3.0	2.9
130904	3.4	4.2	5.2	6.8	11	17	zan1	2.8	2.7
140213	4.8	6.4	8.4	20	39	80	bzn2	3.0	2.9
140311	1.6	2.1	2.8	0.6	0.9	1.3	bwse	2.3	2.3
140318	3.3	4.0	5.1	0.9	1.4	2.4	bmd2	2.1	2.2
140702	2.0	2.7	3.4	0.3	0.5	0.7	boww	2.1	2.2
140809	5.0	6.4	8.4	3.1	5.5	11	boww	2.0	2.1
140901	0.6	1.1	1.7	0.2	0.3	0.5	bapp	2.6	2.8
140930	1.9	2.9	4.2	1.6	3.2	6.1	bhar	2.8	2.8
141105	5.1	6.0	7.4	23	33	55	bmd2	2.9	2.7
150106	1.8	2.6	3.4	0.5	0.9	1.4	bhks	2.7	2.3
150118	3.7	4.6	5.6	0.6	0.9	1.4	bhar	1.5	1.6
150225	2.2	2.9	4.0	1.2	1.8	3.2	bapp	2.3	2.3
150324	1.0	1.4	2.0	0.1	0.2	0.3	bapp	2.3	2.2
150516	2.8	3.5	4.7	0.1	0.2	0.4	bapp	1.6	1.6
150521	0.7	1.4	2.2	0.01	0.03	0.05	bhks	1.8	1.9
150527	1.8	2.5	3.5	0.2	0.3	0.5	buhz	2.0	2.0
150606	3.3	4.1	5.3	0.4	0.7	1.2	bwse	1.9	1.9
150610	3.7	4.9	6.8	0.2	0.4	0.9	bwse	1.8	1.6
150707	5.1	6.8	13	0.9	1.8	13	bhar	2.1	1.8
150930	2.3	3.4	4.9	4.7	8.3	16	bfb2	3.1	2.6
151030	3.8	5.5	7.5	0.7	1.4	3	g200	2.3	1.9

4. Conclusions

Numerous empirical studies have shown that 1:1 scaling between M_L and **M** does not extend to low magnitudes. For $M_L > 3$, the average of the studies seems to conform with $\mathbf{M} \approx M_L$, albeit with significant scatter of the scaling relations between individual regions. For $M_L < 2$, and for studies spanning a broader magnitude range, it is seen that $\mathbf{M} > M_L$. The difference, furthermore, tends to increase for increasingly small magnitudes, with up to a unit of difference for $M_L = 0$ events. Three studies compiling data over a broad magnitude range: in Europe, Switzerland and border regions, and in California, show a distinct curve in the M_L:**M** scaling below $M_L = 3$.

This is consistent with simulation-based studies, which show that when accounting for the effect of attenuation (Q and κ_0) *and the* Wood-Anderson instrument response, we should expect a curvilinear scaling relation between M_L and **M**. This is due to a complex interaction of the earthquake source signal and the filtering effects of the propagation medium (low-pass) and instrument response (displacement high-pass).

Due to the strong regional dependence of M_L assigned for a given earthquake (e.g., Fäh *et al.*, 2011) coupled with the limited datasets containing both M_L and **M**, regional correlations calibrated over limited magnitude ranges are usually applied in PSHA projects. Since it is known that the scaling should not be linear, this means that such conversions are only valid between the range of magnitudes in which they were derived. Given a suitable seismological background model (e.g., Atkinson and Boore, 2006; Rietbrock *et al.*, 2013; Edwards and Fäh, 2013), the expected scaling can be simulated. However, such models are known to be non-unique and, as is often done in PSHA, the epistemic uncertainty of the correction should also be carefully considered.

In the Groningen case it has been shown that above $M_L = 2.5$ that **M** is approximately 0.2 units smaller than M_L. A systematic trend similar to those observed in other empirical and theoretical studies is seen for magnitudes below $M_L = 2.5$, with $\mathbf{M} = M_L$ at $M_L = 1.5$ (Figure), although the dataset is small. The fact that the relationship between the two scales appears to be linear with gradient of unity for magnitudes above 2.5 enables the stochastic simulation approach to be used with some confidence for the GMPE development. However, for several other aspects of the hazard and risk assessment for the Groningen field—including comparisons with models from other regions, adjustments based on other GMPEs, and estimates of M_{max}—adjustments should be made for the 0.2 difference between the M_L values determined by KNMI for induced earthquakes and the corresponding moment magnitudes. Due to the relationship between M_L, **M** and stress parameter, the stress parameter of Groningen earthquakes was calculated. Values were generally low (<50 bar) consistent with the GMPE adopted for the region.

5. References

Abercrombie, R. E. (1995). Earthquake Source Scaling Relationships from-1 to 5 Ml Using Seismograms Recorded at 2.5-Km Depth, *J. geophys. Res* **100**, 24015-24036.

Archuleta, R. J., E. Cranswick, C. Mueller and P. Spudich (1982). Source Parameters of the 1980 Mammoth Lakes, California, Earthquake Sequence, *Journal of Geophysical Research* **87**, 4595-4607, doi: Doi 10.1029/Jb087ib06p04595.

Atkinson, G. M. and D. M. Boore (2006). Earthquake Ground-Motion Prediction Equations for Eastern North America, *Bulletin of the Seismological Society of America* **96**, 2181-2205, doi: Doi 10.1785/0120050245.

Bakun, W. H. and A. G. Lindh (1977). Local Magnitudes, Seismic Moments, and Coda Durations for Earthquakes near Oroville, California, *Bulletin of the Seismological Society of America* **67**, 615-629.

Bakun, W. H. and W. B. Joyner (1984). The M_L scale in central California, *Bulletin of the Seismological Society of America* **74**, 1827-1843.

Bay, F., D. Fäh, L. Malagnini and D. Giardini (2003). Spectral shear-wave ground-motion scaling in Switzerland, *Bulletin of the Seismological Society of America* **93**, 414-429.

Bay, F., S. Wiemer, D. Fäh and D. Giardini (2005). Predictive ground motion scaling in Switzerland: Best estimates and uncertainties, *Journal of Seismology* **9**, 223-240.

Bindi, D., D. Spallarossa, C. Eva and M. Cattaneo (2005). Local and Duration Magnitudes in Northwestern Italy, and Seismic Moment Versus Magnitude Relationships, *Bulletin of the Seismological Society of America* **95**, 592-604, doi: Doi 10.1785/0120040099.

Boatwright, J. (1978). Detailed Spectral Analysis of Two Small New York State Earthquakes, *Bulletin of the Seismological Society of America* **68**, 1117-1131.

Bolt, B. A. and M. Herraiz (1983). Simplified Estimation of Seismic Moment from Seismograms, *Bulletin of the Seismological Society of America* **73**, 735-748.

Bommer, J. J., K. J. Coppersmith, R. T. Coppersmith, K. L. Hanson, A. Mangongolo, J. Neveling, E. M. Rathje, A. Rodriguez-Marek, F. Scherbaum and R. Shelembe (2015a). A SSHAC Level 3 Probabilistic Seismic Hazard Analysis for a New-Build Nuclear Site in South Africa, *Earthquake Spectra* **31**, 661-698.

Bommer, J. J., B. Dost, B. Edwards, A. Rodriguez-Marek, P. P. Kruiver, P. Meijers, M. Ntinalexis and P. J. Stafford (2015b). Development of Version 2 Gmpes for Response Spectral Accelerations and Significant Durations from Induced Earthquakes in the Groningen Field, pp. 515.

Bommer, J. J., B. Dost, B. Edwards, P. J. Stafford, J. v. Elk, D. Doornhof and M. Ntinalexis (2016). Developing an Application-Specific Ground-Motion Model for Induced Seismicity, *Bulletin of the Seismological Society of America* **106**, doi: 10.1785/0120150184.

Boore, D. M. (1983). Stochastic Simulation of High-Frequency Ground Motions Based on Seismological Models of the Radiated Spectra, *Bulletin of the Seismological Society of America* **73**, 1865-1894.

Boore, D. M. (1989). The Richter Scale: Its Development and Use for Determining Earthquake Source Parameters, *Tectonophysics* **166**, 1-14.

Boore, D. M. (2003). Simulation of Ground Motion using the Stochastic Method, *Pure and Applied Geophsyics* **160**, 635-676.

Boore, D.M. and J. Boatwright (1984). Average body-wave radiation coefficients, *Bulletin of the Seismological Society of America* **74**, 1615-1621.

Braunmiller, J., N. Deichmann, D. Giardini, S. Wiemer and S. M. W. Grp (2005). Homogeneous Moment-Magnitude Calibration in Switzerland, *Bulletin of the Seismological Society of America* **95**, 58-74, doi: Doi 10.1785/0120030245.

Brune, J. N. (1970). Tectonic Stress and Spectra of Seismic Shear Waves from Earthquakes, *Journal of Geophysical Research* **75**, 4997-5009.

Brune, J. N. (1971). Correction, *Journal of Geophysical Research* **76**, 5002.

Clinton, J.F., E. Hauksson and K. Solanki (2006). An evaluation of the SCSN moment tensor solutions: robustness of the Mw Magnitude scale, style of faulting, and automation of the method, *Bulletin of the Seismological Society of America* **96**, 1689-1705, doi:10.1785/0120050241

De Lorenzo, S., A. Zollo and G. Zito (2010). Source, Attenuation, and Site Parameters of the 1997 Umbria-Marche Seismic Sequence from the Inversion of P Wave Spectra: A Comparison between Constant Q(P) and Frequency-Dependent Q(P) Models, *Journal of Geophysical Research-Solid Earth* **115**, B09306, doi: Doi 10.1029/2009jb007004.

Deichmann, N. (2006). Local Magnitude, a Moment Revisited, *Bulletin of the Seismological Society of America* **96**, 1267-1277, doi: Doi 10.1785/0120050115.

Dost, B. and H. Haak (2002). A comprehensive description of the KNMI seismological instrumentation, *KNMI technical report*, TR-245, 60pp.

Dost, B. and H. Haak (2007). Natural and Induced Seismicity, *Geology of the Netherlands*, 223-239.

Drouet, S., A. Souriau and F. Cotton (2005). Attenuation, seismic moments, and site effects for weak-motion events: Application to the Pyrenees, *Bulletin of the Seismological Society of America* **95**, 1731-1785, doi: Doi 10.1785/0120040105.

Drouet, S., S. Chevrot, F. Cotton and A. Souriau (2008). Simultaneous Inversion of Source Spectra, Attenuation Parameters, and Site Responses: Application to the Data of the French Accelerometric Network, *Bulletin of the Seismological Society of America* **98**, 198-219, doi: Doi 10.1785/0120060215.

Drouet, S., F. Cotton and P. Gueguen (2010). Nu(S30), Kappa, Regional Attenuation and M-W from Accelerograms: Application to Magnitude 3-5 French Earthquakes, *Geophysical Journal International* **182**, 880-898, doi: DOI 10.1111/j.1365-246X.2010.04626.x.

Edwards, B., B. Allmann, D. Fäh and J. Clinton (2010). Automatic Computation of Moment Magnitudes for Small Earthquakes and the Scaling of Local to Moment Magnitude, *Geophysical Journal International* **183**, 407-420, doi: 10.1111/j.1365-246X.2010.04743.x.

Edwards, B. and D. Fäh (2013). A Stochastic Ground-Motion Model for Switzerland, *Bulletin of the Seismological Society of America* **103**, 78-98, doi: 10.1785/0120110331.

Edwards, B., T. Kraft, C. Cauzzi, P. Kästli and S. Wiemer (2015). Seismic Monitoring and Analysis of Deep Geothermal Projects in St Gallen and Basel, Switzerland, *Geophysical Journal International* **201**, 1020-1037, doi: 10.1093/gji/ggv059.

Edwards, B., A. Rietbrock, J. J. Bommer and B. Baptie (2008). The Acquisition of Source, Path, and Site Effects from Microearthquake Recordings Using Q Tomography: Application to the United Kingdom, *Bulletin of the Seismological Society of America* **98**, 1915-1935, doi: 10.1785/0120070127.

Fäh, D., D. Giardini, P. Kästli, N. Deichmann, M. Gisler, G. Schwarz-Zanetti, S. Alvarez-Rubio, S. Sellami, B. Edwards and B. Allmann (2011). Ecos-09 Earthquake Catalogue of Switzerland Release 2011 Report and Database. Public Catalogue, 17. 4. 2011. Swiss Seismological Service Eth Zurich, pp. 42.

Fletcher, J., J. Boatwright, L. Haar, T. Hanks and A. Mcgarr (1984). Source Parameters for Aftershocks of the Oroville, California, Earthquake, *Bulletin of the Seismological Society of America* **74**, 1101-1123.

Goertz-Allmann, B. P., B. Edwards, F. Bethmann, N. Deichmann, J. Clinton, D. Fäh and D. Giardini (2011). A New Empirical Magnitude Scaling Relation for Switzerland, *Bulletin of the Seismological Society of America* **101**, 3088-3095, doi: 10.1785/0120100291.

Grunthal, G. and R. Wahlstrom (2012). The European-Mediterranean Earthquake Catalogue (Emec) for the Last Millennium, *Journal of Seismology* **16**, 535-570, doi: DOI 10.1007/s10950-012-9302-y.

Grünthal, G. and R. Wahlstrom (2003). An M-W Based Earthquake Catalogue for Central, Northern and Northwestern Europe Using a Hierarchy of Magnitude Conversions, *Journal of Seismology* **7**, 507-531, doi: Doi 10.1023/B:Jose.0000005715.87363.13.

Grunthal, G., R. Wahlstrom and D. Stromeyer (2013). The SHARE European Earthquake Catalogue (SHEEC) for the Time Period 1900-2006 and Its Comparison to the European-Mediterranean Earthquake Catalogue (Emec), *Journal of Seismology* **17**, 1339-1344, doi: DOI 10.1007/s10950-013-9379-y.

Grünthal, G., R. Wahlstrom and D. Stromeyer (2009). The Unified Catalogue of Earthquakes in Central, Northern, and Northwestern Europe (Cenec)-Updated and Expanded to the Last Millennium, *Journal of Seismology* **13**, 517-541, doi: DOI 10.1007/s10950-008-9144-9.

Gutenberg, B. and C. F. Richter (1944). Frequency of Earthquakes in California, *Bulletin of the Seismological Society of America* **34**, 185-188.

Gutenberg, B. and C. F. Richter (1945a). Amplitudes of Surface Waves and Magnitudes of Shallow Earthquakes, *Bulletin of the Seismological Society of America* **35**, 57-69.

Gutenberg, B. and C. F. Richter (1945b). Amplitudes of P, PP and S Waves and Magnitudes of Shallow Earthquakes, *Bulletin of the Seismological Society of America* **35**, 1-12.

Gutenberg, B. and C. F. Richter (1956). Magnitude and Energy of Earthquakes, *Annals of Geophysics* **9**, 1-15.

Haak, H.W. and J.J.A. van Gend (1992). Bepaling van de detectiegrenzen voor het seismisch netwerk rond Assen. *KNMI internal report* SO-92-05.

Hanks, T. C. and D. M. Boore (1984). Moment-Magnitude Relations in Theory and Practice, *Journal of Geophysical Research* **89**, 6229-6235, doi: Doi 10.1029/Jb089ib07p06229.

Hanks, T. C. and H. Kanamori (1979). Moment Magnitude Scale, *Journal of Geophysical Research* **84**, 2348-2350.

Johnson, L. R. and T. V. Mcevilly (1974). Near-Field Observations and Source Parameters of Central California Earthquakes, *Bulletin of the Seismological Society of America* **64**, 1855-1886.

Kanamori, H. (1977). Energy-Release in Great Earthquakes, *Journal of Geophysical Research* **82**, 2981-2987, doi: Doi 10.1029/Jb082i020p02981.

Kanamori, H., J. Mori, E. Hauksson, T.H. Heaton, L.K. Hutton and L.M. Jones (1993). Determination of earthquake energy release and M_L using terrascope, *Bulletin of the Seismological Society of America* **83,** 330-346.

Margaris, B. N. and C. B. Papazachos (1999). Moment-Magnitude Relations Based on Strong-Motion Records in Greece, *Bulletin of the Seismological Society of America* **89**, 442-455.

Richter, C. F. (1935). An Instrumental Earthquake Magnitude Scale, *Bulletin of the Seismological Society of America* **25**, 1-32.

Rietbrock, A., F. Strasser and B. Edwards (2013). A Stochastic Earthquake Ground-Motion Prediction Model for the United Kingdom, *Bulletin of the Seismological Society of America* **103**, 57-77, doi: 10.1785/0120110231.

Roumelioti, Z., C. Benetatos and A. Kiratzi (2009). The 14 February 2008 Earthquake (M6.7) Sequence Offshore South Peloponnese (Greece): Source Models of the Three Strongest Events, *Tectonophysics* **471**, 272-284, doi: DOI 10.1016/j.tecto.2009.02.028.

Sargeant, S. and L. Ottemoller (2009). Lg Wave Attenuation in Britain, *Geophysical Journal International* **179**, 1593-1606, doi: DOI 10.1111/j.1365-246X.2009.04325.x.

Savage, M. K. and J. G. Anderson (1995). A Local-Magnitude Scale for the Western Great Basin-Eastern Sierra Nevada from Synthetic Wood-Anderson Seismograms, *Bulletin of the Seismological Society of America* **85**, 1236-1243.

Strasser, F. (2013). Uniform Estimation of Moment Magnitudes for South African Tectonic Earthquakes, *Unpublished Manuscript*.

Thatcher, W. and T. C. Hanks (1973). Source Parameters of Southern-California Earthquakes, *Journal of Geophysical Research* **78**, 8547-8576, doi: Doi 10.1029/Jb078i035p08547.

USNRC (2012). *Central and Eastern United States Seismic Source Characterization for Nuclear Facilities*, NURGE-2115, US Nuclear Regulatory Commission, Washington DC.

Viegas, G., R.E. Abercrombie and W-Y. Kim (2010). The 2002 M5 Au Sable Forks, NY, earthquake sequence: Source scaling relationships and energy budget, *Journal of Geophysical Research* **115**, B07310, doi: 10.1029/2009JB006799.

York, D., N. M. Evensen, M. L. Martınez and J. D. B. Delgado (2004). Unified Equations for the Slope, Intercept, and Standard Errors of the Best Straight Line, *American Journal of Physics* **72**, 367-375.

Zollo, A., A. Orefice and V. Convertito (2014). Source Parameter Scaling and Radiation Efficiency of Microearthquakes Along the Irpinia Fault Zone in Southern Apennines, Italy, *Journal of Geophysical Research-Solid Earth* **119**, 3256-3275, doi: Doi 10.1002/2013jb010116.

APPENDIX

Sensitivity to the Source Spectrum Model

In the inversions of the Fourier amplitude spectra (FAS) of Groningen ground motions to estimate parameters such as seismic moment, corner frequency and stress drop, a model needs to be assumed for the seismic source spectrum. For the inversions to estimate input parameters for the simulations that underlie the generation of the Groningen GMPEs, the Brune (1970, 1971) spectrum has been used, in common with most simulations for the derivation of stochastic GMPEs. However, in the analyses presented in this report the Boatwright (1978) source spectrum—which is a subtle modification of the Brune spectrum—was used since it was found to give a slightly better fit for the dataset analysed herein. Since this may appear as an important inconsistency, an exploratory analysis was performed using the recordings from the database being used to derive the current versions of the GMPE to determine if there is a definite preference for one source spectrum model over the other.

Using recordings from 24 earthquakes with $M_L \geq 2$, inversions were performed to fit both the Brune and Boatwright spectral models to the FAS after transformation to the NU_B (base of the Upper North Sea formation) rock horizon. The misfit is calculated for each individual FAS as follows:

$$FAS\_misfit = \frac{1}{N}\sum_{1}^{N}\frac{\ln(FAS) - \ln(\mathrm{mod}\,el)}{f} \qquad \text{(A1)}$$

where *f* is frequency, N is number of samples in the FAS. An event specific misfit is the average over all the used FAS for that event:

$$EQ\_misfit = \sum_{1}^{M}\frac{FAS\_misfit}{M} \qquad \text{(A2)}$$

where M is the number of FAS used for the event. In this scheme, the larger the misfit, the poorer the performance of the model in reproducing the recorded FAS. Figure A1 shows a plot of the ratios obtained with the Boatwright spectrum to those obtained with the Brune spectrum for each event, plotted against magnitude. A ratio of less than unity implies a greater misfit with the Boatwright model than with the Brune model. As can be seen from the plot, there is no consistent pattern in terms of superior performance and it can be seen that the use of either of the models is justified (with a possible slight preference for the Brune model at larger magnitudes).

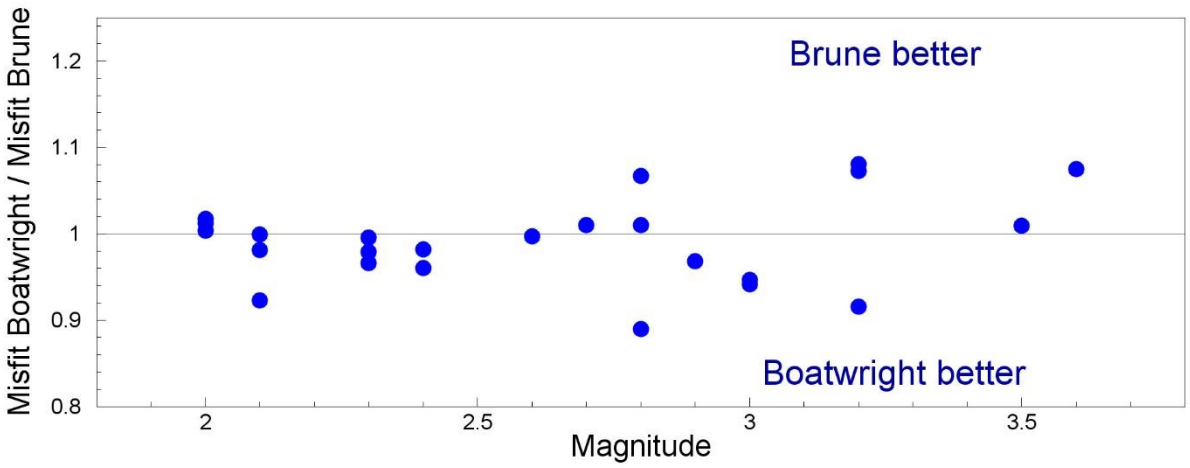

Figure A1. Ratios of misfits obtained fitting the Boatwright model to those obtained using the Brune spectrum